AD_____

GRANT NUMBER DAMD17-96-1-6010

TITLE: Microvasculature Magnetic Resonance Imaging for the
         Diagnosis of Breast Cancer

PRINCIPAL INVESTIGATOR: Cynthia F. Maier
                          Brian K. Rutt, Ph.D.

CONTRACTING ORGANIZATION: John P. Robarts Research Institute
                            London, Ontario, Canada   N6A 5K8

REPORT DATE: October   1998

TYPE OF REPORT: Final

PREPARED FOR: Commander
                U.S. Army Medical Research and Materiel Command
                Fort Detrick, Frederick, Maryland   21702-5012

DISTRIBUTION STATEMENT: Approved for public release;
                          distribution unlimited

The views, opinions and/or findings contained in this report are
those of the author(s) and should not be construed as an official
Department of the Army position, policy or decision unless so
designated by other documentation.

19990811 142

REPORT DOCUMENTATION PAGE

Public reporting burden for this collection of information is estimated to average 1 hour per response, including the time for reviewing instructions, searching existing data sources, gathering and maintaining the data needed, and completing and reviewing the collection of information. Send comments regarding this burden estimate or any other aspect of this collection of information, including suggestions for reducing this burden, to Washington Headquarters Services, Directorate for Information Operations and Reports, 1215 Jefferson Davis Highway, Suite 1204, Arlington, VA 22202-4302, and to the Office of Management and Budget, Paperwork Reduction Project (0704-0188), Washington, DC 20503.

1. AGENCY USE ONLY (Leave blank)	2. REPORT DATE October 1998	3. REPORT TYPE AND DATES COVERED Final (1 May 96 - 31 Oct 98)

4. TITLE AND SUBTITLE Microvasculature Magnetic Resonance Imaging for the Diagnosis of Breast Cancer	5. FUNDING NUMBERS DAMD17-96-1-6010
6. AUTHOR(S) Cynthia F. Maier Brian K. Rutt, Ph.D.	

7. PERFORMING ORGANIZATION NAME(S) AND ADDRESS(ES) John P. Robarts Research Institute London, Ontario, Canada N6A 5K8	8. PERFORMING ORGANIZATION REPORT NUMBER

9. SPONSORING/MONITORING AGENCY NAME(S) AND ADDRESS(ES) Commander U.S. Army Medical Research and Materiel Command Fort Detrick, Frederick, Maryland 21702-5012	10. SPONSORING/MONITORING AGENCY REPORT NUMBER

11. SUPPLEMENTARY NOTES

12a. DISTRIBUTION / AVAILABILITY STATEMENT Approved for public release; distribution unlimited	12b. DISTRIBUTION CODE

13. ABSTRACT (Maximum 200

The development of noninvasive methods for characterizing mammographically indeterminate lesions represents an active area of current research in medical imaging. In particular, much research effort is being directed toward the development of new techniques for measuring tumour blood flow. This thesis consists of experiments designed to evaluate the use of a magnetic resonance imaging technique called Intravoxel Incoherent Motion (IVIM) to produce microvascular flow images of breast lesions.

14. SUBJECT TERMS Breast Cancer			15. NUMBER OF PAGES 52
			16. PRICE CODE

17. SECURITY CLASSIFICATION OF REPORT Unclassified	18. SECURITY CLASSIFICATION OF THIS PAGE Unclassified	19. SECURITY CLASSIFICATION OF ABSTRACT Unclassified	20. LIMITATION OF ABSTRACT Unlimited

NSN 7540-01-280-5500

FOREWORD

Opinions, interpretations, conclusions and recommendations are those of the author and are not necessarily endorsed by the U.S. Army.

_____ Where copyrighted material is quoted, permission has been obtained to use such material.

_____ Where material from documents designated for limited distribution is quoted, permission has been obtained to use the material.

_____ Citations of commercial organizations and trade names in this report do not constitute an official Department of Army endorsement or approval of the products or services of these organizations.

✓ In conducting research using animals, the investigator(s) adhered to the "Guide for the Care and Use of Laboratory Animals," prepared by the Committee on Care and use of Laboratory Animals of the Institute of Laboratory Resources, national Research Council (NIH Publication No. 86-23, Revised 1985).

✓ For the protection of human subjects, the investigator(s) adhered to policies of applicable Federal Law 45 CFR 46.

NA In conducting research utilizing recombinant DNA technology, the investigator(s) adhered to current guidelines promulgated by the National Institutes of Health.

NA In the conduct of research utilizing recombinant DNA, the investigator(s) adhered to the NIH Guidelines for Research Involving Recombinant DNA Molecules.

NA In the conduct of research involving hazardous organisms, the investigator(s) adhered to the CDC-NIH Guide for Biosafety in Microbiological and Biomedical Laboratories.

_____   Oct. 21 '98
PI - Signature   Date

Table of Contents

Cynthia Maier – Final Report for DAMD17-96-1-6010

1. Introduction

1.1 Diagnosis of Breast Cancer

X-ray mammography is the current gold standard in breast imaging and, in combination with a physical exam, detects breast cancer with a sensitivity of 85-95%. [1,2] Diagnosis of detected focal abnormalities is based primarily on morphological features such as boundary appearance, presence or absence of spiculations, and distribution and size of calcifications. Some lesions can be characterized specifically as either benign or malignant on the basis of these features alone; however, many are indeterminate, and require further evaluation. [3,4] Recent trials have shown that 70-80% of mammographically indeterminate lesions that progress to surgical biopsy are benign. [4-7] For women with particularly dense breast tissue and/or fibrocystic changes, the false positive rate for x-ray mammography can be as high as 90%. [5,8] For these women, the surgical biopsy serves only to provide a diagnosis since it is not necessary to remove a benign lesion unless it is causing pain.

Recently, less invasive biopsy techniques have been developed which use a large diameter needle fitted with a cutting device to extract cores of tissue from a lesion for histological analysis. In the case of a solid, palpable lesion, core biopsy is sometimes used to provide a definitive diagnosis even in the case of a negative result; however, this application is still very controversial. [9-12] Although the reported accuracy of this core biopsy technique in small studies has improved rapidly since its inception (largely because of improved sampling accuracy using needle guidance by imaging methods), a conservative approach demands more extensive testing in large populations with surgical confirmation before a meaningful evaluation of its reliability can take place. [13]

Development of accurate, non-invasive methods for characterizing mammographically indeterminate lesions represents an active area of current research in medical imaging. Ideally, a new diagnostic test would have reliably low false negative rates and would significantly reduce the number of surgical biopsies for benign lesions currently being performed; however, even if the false-negative rate associated with the test were unacceptably high, a non-invasive test with high positive predictive value for malignancy would have a profound impact on current surgical practice for breast cancer. At present, patients undergo surgical biopsy, then return for a second surgical procedure if the biopsy is positive, allowing time for patients to assess their treatment options in the intervening weeks. A non-invasive predictor of malignancy could eliminate this two-step procedure, reducing the risk of disease progression and the psychological stress of delaying treatment.

1.2 Patient Prognosis

In 1990, Fearon and Vogelstein published their work elucidating the genetic steps to malignancy in colon cancer. [14] It is now widely believed that breast cancer also evolves in a similar way from normal ductal epithelium, to hyperplasia, to atypical hyperplasia, to carcinoma *in situ* and finally to invasive carcinoma. [15] At each stage in this progression away from normal epithelium toward malignancy and invasion, the prognosis for the patient worsens. Following a surgical biopsy, the extent of malignant transformation is determined and the metastatic potential of a tumour evaluated to best determine clinical treatment.

The recent technical improvements in mammography and increase in the number of women who undergo screening have dramatically shifted the stage of cancers seen at pathology.

Approximately 66% of patients with newly detected breast cancer will have no detected lymph node involvement, and 20-30% of these newly-detected lesions will be found while still confined within a duct. [4,6] Fifteen to twenty per cent of node-negative patients with invasive carcinoma will relapse in the 10 years following surgery. [16] Currently, there is no proven technique for identifying this high-risk subpopulation within the node-negative group. For these women, standard pathological indicators such as tumour size, histologic differentiation, and hormone receptor status have shown variable correlation with disease recurrence and patient survival. [17] For these localized breast cancers, surgical removal of the tumour supplemented by radiation therapy has replaced mastectomy for many women. [18,19] The development of prognostic indicators to identify patients from this group who are likely to benefit from systemic chemotherapy is also an active and important area of current research. Currently, there are no accepted guidelines for clinical treatment of women with ductal carcinoma in situ (DCIS). [20] Clinical care of patients with early-stage breast cancer is controversial, and the development of a test to assess the metastatic potential of these lesions is an important area of research in breast pathology.

A large body of recent work exists concerning the development of new prognostic indicators for early-stage carcinomas. The list of new markers currently being evaluated is long and growing. New markers which show promise are those reflecting cellular characteristics such as DNA content, ploidy (define), cell cycle status, and proliferation indices. In addition, new genetic tests are being created to evaluate the expression of oncogenes. For example, the tumour suppressor p53 gene has been receiving much attention as a prognostic indicator. Overexpression of the p53 mutant form has been found to correlate with high proliferative activity and disease recurrence in some studies. [21] Unfortunately, these relationships have not been found in all cases, [22] and this new area of research is in need of more concrete results before these indicators can be used routinely for clinical decision-making. None of the multitude of currently available prognostic tests are sufficiently reliable for predicting relapse or survival, and decisions about patient care must be made by weighing many prognostic indicators, in addition to assessing individual patients' needs.

1.3 Tumour Angiogenesis

Tumour progression is known to be dependent on the ability to stimulate the growth of new blood vessels. [23] This process, known as tumour angiogenesis, is integral to all solid malignant neoplasms, and is required in order to supply nutrients and oxygen to the expanding tumour. In tumour spheroids, transport of nutrients and oxygen by diffusion was shown to limit tumour growth to a size of 1-2 mm diameter. [24-26] In a chick embryo model, however, implanted tumour cells were shown to stimulate the growth of new blood vessels, and to thereby achieve rapid growth beyond this diffusion-limited size constraint. [27] It was therefore believed initially that the switch to an angiogenic phenotype would occur when a tumour reaches its maximum diffusion-limited growth potential. More recent results have indicated that the onset of angiogenesis can occur much earlier in tumour progression, and may even occur well before the switch to a malignant phenotype. [28] Recent studies evaluating microvessel density around in situ breast carcinoma have shown increased vascularity even around these very early stage lesions. [29-31] More strikingly, cells extracted from premalignant lesions have demonstrated the ability to induce new vessel formation in model tissue systems. Using a rabbit cornea assay, cells extracted from atypical hyperplasia and even from histologically normal lobules from cancerous breasts have been shown to stimulate angiogenesis. [32-35] Although these results are preliminary, and mechanisms of angiogenesis are still not fully understood, it is evident that even very early malignancies, and some premalignant

lesions undergo marked changes in vasculature.

1.3.1 Implications for Diagnosis: It has been hypothesized that the characteristic new vessel growth associated with tumour angiogenesis could allow differentiation between malignancies and benign breast lesions using medical imaging techniques. [36-40] Specifically, it has been speculated that the number of small vessels per unit volume of tissue (microvessel density) would be higher for malignant lesions. Some imaging researchers have even asserted that benign lesions are not expected to be vascularized at all, and that the detection of blood flow around a lesion would therefore strongly indicate malignancy. Although many attempts premised on this assumption have been made to diagnose breast disease using IR thermography, positron emission tomography, Doppler ultrasound, and magnetic resonance imaging techniques, none of these studies has achieved the highly reliable differentiation between benign and malignant lesions that was expected. This has led some authors to suggest that the absolute number of microvessels in benign and malignant lesions may overlap in some cases. More hopefully, several recent imaging studies have suggested that an increased number of these vessels specifically in the lesion periphery may be a characteristic that is uniquely associated with malignancy. [41,42]

To date, most studies evaluating microvessel density in breast using histological techniques have focussed on invasive breast carcinomas, and the increased number of blood vessels associated with a strong tendency to metastasize. Although comparisons of microvessel density to normal breast tissue have been made, relatively few of these studies have included benign breast lesions, and very little data about vascularity in benign tumours is actually available. The hypothesis of benign lesions being avascular appears to have been based almost solely on what is known about breast cancers, extrapolating through "less invasive" to "benign". If the number of blood vessels or their spatial distribution around malignant lesions is, in fact, characteristic for malignancy, a non-invasive measure of blood flow around an indeterminate lesion would add valuable information to a diagnostic work-up; however, histological studies evaluating distributions of vessels in benign lesions are certainly required to test this hypothesis.

1.3.2 Implications for Prognosis: The entry of cancer cells into the bloodstream and subsequent formation of distant metastases is facilitated by the increasing number of small new blood vessels around the tumour as it grows. Studies of patients with invasive breast carcinoma have shown that the number of microvessels in angiogenic "hotspots" in the tumour periphery correlates strongly with the extent of metastatic progression. [43-47] In one study, each 10-fold increase in the number of microvessels per x200 microscope field corresponded to a 1.6-fold increase in the risk of metastasis. [43] The number of microvessels in these hotspots has also been shown to outperform lymph-node positivity as a predictor for the development of distant metastatic disease. [44-46] Moreover, micro-vessel density is the only prognostic indicator that is a statistically significant predictor of overall survival for node-negative women. [44,47] A non-invasive diagnostic technique that measures microvessel density in invasive carcinomas would identify node-negative lesions with high metastatic potential and would immediately indicate which patients are most likely to benefit from adjuvant systemic therapy.

A measurement of microvessel density may also have value in prognosis for *in situ* carcinoma and for premalignant disease. It has been proposed that the degree of angiogenic activity around premalignant lesions and early-stage cancers may be an indicator of which lesions will progress to more invasive disease. [48] Preliminary results from a retrospective study by Guinebretiere [49] showed that vessel density around hyperplastic lesions correlated with risk for subsequent development of invasive carcinoma and, further, that vessel density had a higher

prognostic value than atypia. A non-invasive method for measuring microvessel density around premalignant lesions and in situ cancers may provide early identification of lesions that have the potential to progress to more invasive disease, and require more aggressive therapy, or long-term patient follow-up.

1.4   Magnetic Resonance Imaging (MRI)

Breast imaging using MRI has several advantages over x-ray mammography: (a) image contrast can be based on one or more of several independent tissue parameters (T1, T2 and water content) and can therefore be manipulated to optimize contrast between lesions and normal parenchymal tissue, (b) optimal display of tissue close to the chest wall can be obtained, since no compression of the breast is required, (c) images are obtained either as 2-dimensional slices in any orientation, or as 3-dimensional volumes, eliminating overlap of internal breast structures on the image.

The focus of research in MR imaging of the breast has been on contrast-enhanced studies. It was originally believed that these contrast exams would distinguish malignant lesions from benign tumours with a high degree of reliability, since microvessels associated with malignant lesions were thought to be more numerous and more permeable than in normal tissue. Initially, simple snapshot "before" and "after" images were acquired, and areas of focal enhancement were evaluated for percentage signal increase. These MR studies reported detection of breast cancer with high sensitivity; however, diagnostic specificity was widely variable across different studies (20-85%). [50-53] Most solid malignancies showed marked contrast enhancement, allowing easy differentiation from mammographically similar features such as cysts, old scar tissue, and dense normal breast tissue. Unfortunately, some benign diseases such as atypical hyperplasia and fibroadenomas showed similar absolute enhancement to malignancies, and some malignancies demonstrated benign-type enhancement.

Despite widespread efforts to refine MR techniques and analysis of these contrast-enhanced studies, little improvement in specificity resulted. [39,42,54-56] Extremely high sensitivity to cancer using this method is reported (94-100%); unfortunately, a large number of false positives has also been reported, where the majority of enhancing benign lesions are fibroadenomas or fibrocystic change.

Recently, new MR hardware has become commercially available that allows higher spatial resolution imaging (300-700μm in-plane resolution with 2-3 mm slice thickness). This improved resolution allows more detailed evaluation of lesion borders, and internal structure. In an initial study of patients with a palpable or mammographically visible mass, a high spatial resolution image was obtained before contrast agent injection, a series of lower spatial resolution images was acquired rapidly during the first 4-7 minutes post-injection to obtain high temporal resolution enhancement curves, and a second high spatial resolution image was then acquired using identical parameters to the first image. [41] These preliminary high spatial resolution contrast imaging results have indicated that the additional information about architectural features <u>combined</u> with initial slope calculations may result in increased specificity for breast cancer. Specifically, it was found that malignancies tended to demonstrate higher contrast enhancement around the lesion periphery and also tended to have spiculated borders, whereas benign lesions such as fibroadenomas exhibited a more diffuse, uniform enhancement with smooth borders. In a further study looking specifically at patients with DCIS, this technique detected ten of thirteen DCIS lesions, where three of the ten identified lesions were not visible on mammography. [57] These results have demonstrated considerable promise for combining information about tumour blood flow with high-resolution imaging techniques.

Although initial high-spatial resolution contrast-enhanced imaging results are promising, a fundamental problem with contrast-enhanced methods is that the signal enhancement seen reflects two inseparable aspects of tumour blood vessels: total vessel surface area within a voxel, and vessel permeability. Moreover, contrast exams are expensive and contrast agents are not well-tolerated by all patients. A non-invasive technique that is sensitive to only one aspect of the vasculature e.g. blood flow rate provides simpler interpretation.

The goal of this thesis was to test the feasibility of using the Intravoxel Incoherent Motion Imaging technique (IVIM) to measure microvessel blood flow around human breast lesions. IVIM is essentially a modification of an established protocol used for over thirty years to measure small water motions due to diffusion. In IVIM imaging, the same motion-sensitive protocols are used, where the protocols are tuned for sensitivity to the motion of the water component of blood flowing in small vessels. The IVIM technique has been demonstrated to be sensitive to blood flow in microvessels in the brain [58], and provides two quantitative measures: 1) absolute determination of the average blood flow velocity in these vessels within each tissue voxel, and 2) a relative measure of the total amount of blood flowing in these vessels at the time the image was acquired. It is possible that the measurement of these parameters in breast tissue may provide valuable information about microvessel densities and distributions around breast lesions.

The thesis outline was as follows: 1) The hypothesis that spatial distributions of blood vessels around a solid breast lesion are specific for malignancy was tested in a study of archival biopsy tissue stained for blood vessels; 2) The IVIM method was evaluated using a mouse tumour model; 3) Hardware necessary for the application of the IVIM technique (or diffusion imaging) to human breast cancer in a clinical setting was designed, constructed and tested for feasibility.

2. Distributions of Microvessels in Breast Lesions

A comparison study of spatial distributions of microvessels in human breast carcinomas and in fibroadenomas was carried out. Fibroadenomas were selected from other forms of benign breast disease for comparison to carcinomas because MR contrast enhancement patterns can often mimic those seen in invasive cancers. Moreover, fibroadenomas are the most commonly occuring benign solid lesion, and constitute 30-50% of benign lesions seen at surgical biopsy. [59]

Cases were selected from the files of the Department of Pathology at the London Health Sciences Centre, and were stained using Factor VIII-related antigen to identify endothelial cells. Microvessels were counted on x200 magnification in 10 fields in the lesion periphery, and 10 fields in the lesion centre. Where normal tissue was present, microvessels were also counted in 5 fields. The lesion periphery was easily identified on fibroadenomas as an enclosing fibrous capsule, and was defined as the leading edge of invading cells for the invasive carcinomas. Vessels were identified according to the criteria of Weidner et al. [43] where even a single stained endothelial cell was counted as a vessel.

A number of interesting results were obtained from this work. Many of the fibroadenomas in our sample contained, on average, more microvessels than some of the invasive carcinomas we looked at. This finding directly contradicts the assertion by imaging researchers that benign breast lesions are not vascularized, and also explains, to some extent, the overlap in imaging characteristics seen for fibroadenomas and breast cancers. On a more optimistic note, our findings revealed that the numbers of small vessels were higher around the boundaries of invasive carcinomas, whereas these small vessels were more uniformly distributed in fibroadenomas. This characteristic spatial distribution of blood vessels may allow differentiation between fibroadenomas and carcinomas using non-invasive imaging methods sensitized to flow in microvessels. A secondary, but interesting observation was that for the three women aged forty or older who had

fibroadenomas, microvessel density in the surrounding normal breast tissue was extremely high compared with all other women in the fibroadenoma group (for the women with breast cancer, no "normal" tissue was present).

A manuscript describing this work has been accepted for publication in the journal Radiology as: K. Weind, C.F. Maier, B.K. Rutt, M.Moussa, "Comparison of Microvessel Distributions in Invasive Carcinomas and Fibroadenomas of the Breast" (included as Appendix 1). Portions of this work have also been presented at the Annual Meeting of the United States and Canadian Academy of Pathology, Orlando, FL, March 1997; and at the 1997 Annual Meeting of the Radiological Society of North America (RSNA).

3: **Diffusion Imaging in Implanted Human Breast Tumours**

Quantitative diffusion measurements were performed in tumours arising from inoculation of nude mice with human breast cancer cells to determine values for the Apparent Diffusion Coefficient for various components of solid tumours. Diffusion maps were compared to histology, and correlated well with gross tumour morphology. These diffusion measurements were carried out to provide a foundation for the implementation of IVIM experiments in these tumours, by characterizing the behavior of the signal arising from the static spins within the tissue. While these experiments were undertaken as a stepping-stone to IVIM imaging, the results are significant for researchers in cancer therapy, and show that the degree of necrosis resulting from a particular therapy can be monitored non-invasively using MRI.

These experiments were carried out under the supervision of Dr. Degani, Dr. Rutt, and Dr. Bendel. All experiments were performed at the Weizmann Institute of Science in Rehovot, Israel in the lab of Dr. Degani, and this work was completed prior to funding by the U.S. Army Predoctoral Fellowship award. In addition to providing details related to water diffusion in tumours necessary for planning the IVIM experiments, this work was highly valuable as a learning experience. By performing these experiments in Dr. Degani's lab, I was able to benefit from her years of experience working with this tumour cell line in nude mice, and also from Dr. Bendel's MR imaging expertise.

Ideally, IVIM experiments would have also been undertaken in Dr. Degani's lab; unfortunately, the limited length of my stay there (4 1/2 months) did not allow for the extensive software and hardware testing that is required for such sensitive work. Diffusion imaging alone is highly demanding on MR system performance, and the ability to reliably extract information about 5-10% of the collected signal requires thorough and meticulous system evaluation. We chose instead to continue the work here in London, Ontario, on our newly acquired 4 Tesla whole-body imager.

A paper describing this work (included as Appendix 2) has been published as: C.F. Maier, Y. Paran, P. Bendel, B.K. Rutt, H. Degani, "Quantitative Diffusion Imaging in Implanted Human Breast Tumours". Magnetic Resonance in Medicine, **37**, pp.576-581, 1997. This work was also presented at the 4th Meeting of the International Society for Magnetic Resonance in Medicine, New York City, NY, April 1996.

4: **IVIM Imaging in Implanted Tumours**

In 1986, Le Bihan recognized that under certain conditions, blood flow in randomly oriented capillaries could be considered as a "pseudo-diffusion" process and proposed using the PGSE method to visualize this microcirculatory. [58] This application of the PGSE sequence to imaging flow in capillaries was called Intravoxel Incoherent Motion Imaging, because the condition for this flow to mimic a diffusion process is that the flow within a voxel be "incoherent" with

respect to the imaging time.

For voxel-sizes that can be obtained clinically ($1mm^3$-$10mm^3$), we expect to find thousands of capillaries, with a more or less random distribution of orientations. Flow in these vessels therefore resembles a random-walk or pseudo-diffusive motion which can be characterized by an ADC. The relationship of this ADC to the vascular geometry is governed by the flow velocity of water molecules inside the vasculature. If the length of time between diffusion-encoding pulses, Δ, is small, the average velocity can be derived directly from the ADC and is not dependent on the capillary network geometry. To ensure that this requirement is met, it is important to use high gradient strengths for large values of b (rather than increasing b by extending Δ). Additionally, the use of large, short g pulses allows imaging with short TE, so that little signal loss occurs from T2 decay during the imaging sequence.

The total signal arising from a voxel consists of a contribution from spins flowing in the microcirculation (5-10% of total signal) and from spins undergoing Brownian diffusion in the tissue (90-95% of total signal). This signal will exhibit a biexponential decay when plotted against increasing values of b. The fraction of all MR-visible spins within a voxel which are moving in the microcirculation can be determined experimentally from this curve by comparing the amount of signal attenuation due to fast decay (area under the exponential characterized by D^*) to the amount of signal attenuation from the "static component" (area under the exponential characterized by D, the ADC describing tissue water diffusion). Although this D^* decay is due to the spins that are moving within the microcirculation, and does not contain a contribution from static spins inside the vasculature, it is expected that the fraction of moving spins determined will be related to the density of capillaries within the tissue voxel.

Since the publication of Le Bihan's work, much controversy has surrounded the IVIM theory, and Le Bihan's experimental results. The strongest evidence in support of IVIM has been the observation of biexponential signal decay curves, and the derivation of biologically reasonable flow fractions and velocities from these curves. [60-65] Unfortunately, these results have not been reproduced reliably in all studies undertaken to test this technique. [66,67] Others have pointed out the inherent difficulties of fitting data to a biexponential function, and estimated that the signal-to-noise in these experiments was not high enough to derive flow parameters reliably. [68] Many investigators have argued that the source of the biexponential decay is more likely to be macroscopic motions, such as involuntary patient movement, pulsatile brain motion, or CSF flow. [69,62] Others have taken issue with Le Bihan's proposed relationship between the pseudodiffusion coefficient, D^*, and the microvascular geometry and flow parameters, and have developed more complex models to describe the decay curves. [70,71]

The goal of this study was to perform preliminary investigations evaluating the possibility of implementing PGSE-based IVIM for imaging breast tumours. In these experiments, we attempted to control as many of the potential problems with IVIM measurements as possible by using an animal model and MR system in which the vascular signal and signal-to-noise could be maximized, and macroscopic movements minimized. First, to maximize the size of the microvascular signal, we chose a tumour model that was known *a priori* to be highly vascularized. Secondly, mice were anaesthetized using an inhalation anaesthetic, isofluorane, that is known to have minimal effect on tumour blood flow. An rf coil was specially constructed to give excellent B_1 uniformity and signal-to-noise, and further, extensive system characterization was performed using phantoms to ensure optimal system performance.

4.1   Methods
4.1.1   Evaluation of System Performance

In normal tissue, the number of spins within the microcirculation contributing to an MR image is a small fraction (< 5%) of the total number of MR-visible spins. This fraction is slightly higher for well-vascularized tumours, but is not expected to exceed 10%. Because the total MR signal arises from a superposition of the signals from the spins that are flowing in the vascular compartment and the spins that are undergoing molecular diffusion in the tissue, any experiment attempting to isolate a signal from the "flowing fraction", f, requires careful attention to experimental design details and rigorous system testing.

One of the most significant causes of inaccuracy in diffusion imaging are the cross-term contributions from imaging gradients and diffusion gradients. [72,73] These terms were minimized for our pulse sequence by moving the readout compensation pulse from its normal location before the 180° pulse to immediately before the acquisition window. The size of the remaining cross-terms was evaluated in the following way: two sets of PGSE images of a water phantom were acquired for all possible image orientations, with five diffusion-weightings ranging between b = 1 s/mm^2 and b = 450 s/mm^2, and each set acquired with both positive and negative diffusion gradients. The difference in D calculated with images acquired using positive gradients and with those acquired using negative gradients is a sensitive indicator of the presence of imaging gradient cross-terms.

A standard PGSE sequence was used with TE/TR = 56ms/2000ms, Δ=30ms, δ=13ms (Δ and δ are defined as in Figure 1). Images were acquired on a Varian/Siemens Unity INOVA 4 Tesla whole-body MR imager equipped with 25 mT/m gradient coils (the maximum gradient strength available at the duty-cycle required for our pulse sequence was 22 mT/m), using a custom-built 4.5 cm diameter quadrature birdcage rf coil. For our PGSE experiments, gradients were applied simultaneously along all three axes, thereby increasing the diffusion gradient strength by a factor of $\sqrt{3}$ to 38 mT/m. The maximum available gradient strength, together with the longest Δ possible for this TE gave a diffusion weighting of b = 450 s/mm^2. A 5 cm field of view was qualitatively judged to give adequate spatial resolution for depiction of anatomical detail in the mouse. The choice of a 128 x 256 matrix size (6 mm thickness) with TR = 2 s required approximately 4.5 min per diffusion-weighted image. For all experiments, the rf coil and mouse (or phantom) were mounted on a separate, distinct holder which was completely mechanically isolated from the rest of the system. The function of this holder was to isolate the volume being imaged from any system noise due to gradient coil or coldhead vibrations. [74]

To test the stability of the system over an approximately one-hour scan time, preliminary tests with a doped-water phantom were performed. The water phantom used in these experiments consisted of a 20cc plastic syringe (approximately 2 cm in diameter) that was filled with 1mmol MnCl in 0.9% saline. Images of the phantom were acquired continuously for 1.25h (with the parameters described above), toggling back and forth between minimum and maximum diffusion-weightings: g = 1 mT/m (b = 1 s/mm^2), and g = 38 mT/m (b = 450 s/mm^2). The phantom was maintained at 29 +/- 0.5 °C throughout the experiment by the use of several electrical resistance heating pads which lined the main magnet bore at the location of the rf coil.

Images were transferred to a Sun Microsystems ULTRA SPARC 1/140 workstation for analysis using MATLAB software Version 5.0 (The Mathworks, Inc. Natick, MA, USA). Mean signal intensities and standard deviations were measured inside a ROI defined in the phantom.

4.1.2   MRI Measurements in a Tumour Model

B16F1 murine melanoma cells were cultured as described previously. [75] Four- to six-week-old female nude mice were injected subcutaneously in the flank with 1 x 10^5 cells in a volume

of 0.1 ml of medium. This cell line is known to form well-vascularized tumours rapidly. Two groups of six mice each were injected with cancer cells. Tumours were allowed to grow for two to three weeks after injection of cells to sizes of approximately 0.7 to 1 cm in diameter. Mice were provided with food and water *ad libitum.*

Isofluorane, an inhalation anaesthetic known to have minimal effects on the cardiovascular system and tumour blood flow, [76] was used to anaesthetize the mice during imaging. To anaesthetize a mouse for set-up prior to the MRI exam, the mouse was enclosed for approximately 10 to 15 min in a container filled with 1 to 2% isofluorane vapour in oxygen. The mouse was then placed on a small acrylic holder, and paper surgical tape was used to hold the mouse in position during the MR exam, with particular attention paid to restraining the tumour-bearing flank without impairing breathing, or blood flow to the tumour. The mouse and holder were then placed inside a 4.5 cm diameter quadrature birdcage coil built on an acrylic cylinder. The ends of this cylinder were sealed, and a mixture of oxygen and isofluorane vapour was circulated through the coil. Normal thermia was maintained during the experiments using the resistance heating pad arrangement described above. After initial set-up and localization images, transverse-orientation PGSE images of a tumour slice were obtained for approximately 1.25h, according to the pulse sequence protocol described above in §4.1.1.

4.2 Results
4.2.1 Evaluation of System Performance

Diffusion measurements obtained in the water phantom were extremely accurate and reproducible. Exponential diffusion decays were obtained using five diffusion-weighted images for each image orientation, and gradient polarity. These curves were plotted for each imaging slice from the mean signal intensities within an ROI defined inside the phantom. Diffusion coefficients were calculated for all slices from a least-mean-squares fit of the natural logarithm of these data to the diffusion b factors. Results are shown in Table 1 for calculated diffusion coefficients for all possible image orientations and both diffusion gradient polarities.

Table 1 Measured Diffusion Coefficients in a H_2O Phantom at Room Temperature

Slice Orientation	Diffusion Gradient Polarity	D (x10^{-3} mm^2/s)
transverse	+	2.18 +/- .01
transverse	-	2.20 +/- .01
transverse	gm[†]	2.19 +/- .01
sagittal	+	2.13 +/- .01
sagittal	-	2.22 +/- .01
sagittal	gm	2.18 +/- .01
coronal	+	2.14 +/- .01
coronal	-	2.22 +/- .01
coronal	gm	2.18 +/- .01

† D calculated from geometric mean of signal intensities according to the method of Neeman et al. [72]

In initial experiments using the doped-water phantom placed on the patient table, reproducible results could not be obtained. The signal intensity was inconsistent from scan to scan and variations as large as +/- 50% were observed in the measured D. The source of these errors was attributed to vibrations of the patient table, which is indirectly mechanically coupled to the gradient coils through the table supports. These effects were most readily observed in highly diffusion-weighted images (i.e. large gradient amplitudes) as ghosting in images and strong smearing in the phase-encode direction. This kind of structured system noise has been observed previously by Conturo et al. [74] on another Siemens system with a similar patient table configuration as the 4 Tesla scanner used in this study (Siemens Magnetom Vision 1.5 Tesla scanner).

Figure 2 shows results from the 1.25 hour scanning protocol described in §4.1.1. In these experiments, the phantom was mounted in isolation from the system using the custom-built holder. The data plotted corresponds to the mean signal intensity inside a ROI defined over the whole phantom (error bars = +/- SEM). The small standard errors (which are on the order of the size of the plotting symbols), and temporal stability of these signal intensities indicate the extremely high level of system performance achieved with this scanner. The diffusion coefficient calculated from these measurements, 2.45×10^{-3} mm^2/s agrees with literature values for water at 29°C. [77]

4.2.2   MRI Measurements in a Mouse Tumour Model

Images of tumours in four different mice were acquired according to the protocol described in §4.1.2. Although typical signal-to-noise on these images was excellent, (S/N $\approx$ 400:1 for b = 1 s/mm^2, compared to S/N $\approx$ 250:1 for b = 450 s/mm^2 where noise was estimated as the standard deviation in a ROI in the background), phase smearing from motion was obvious. The signal intensity measured in a region of obvious phase smearing ranged from approximately 5% to 25% of the signal intensity within the tumour for the low and high b factor images respectively. In addition to motion artifacts in the images, more significant motions over the course of the exam were evident from visual inspection of the images. Figure 3 shows a typical timecourse of measured signal intensities from a mouse tumour for the 1.25 hour scanning protocol. The data plotted correspond to the mean signal intensity inside a ROI defined within the tumour (error bars = +/- SEM). Comparison to Figure 2 demonstrates the inaccuracy of the results obtained for the mouse. This variability is easily explained by the presence of significant motion ghosts and phase-smearing in the images. ADCs calculated from consecutive pairs of these images varied by approximately 13%.

4.3   Discussion

PGSE imaging using a doped-water phantom produced artifact-free images with extremely high reproducibility and accuracy. In Table 1, calculated diffusion coefficients are given for all three image orientations. Because the diffusion gradients are applied along all three axes, the diffusion coefficients for positive or negative gradient polarities should be the same regardless of the image orientation. The small differences observed (less than 3%) are likely to be due to eddy currents. Eddy currents are different for the three gradient coils, and also depend on the direction of the applied current. They therefore contribute differently to the diffusion-weighting b-factor for each of the imaging orientations and gradient polarities through their interaction cross-terms with the imaging gradients.

For mouse imaging, macroscopic motions during the image acquisitions resulted in

unacceptable phase-smearing and image-to-image misregistration. The mouse tumour model was chosen for our experiments because of the prior, published data from other groups studying the effects of isofluorane on blood flow in solid tumours in mice. The effect of anaesthetic can vary dramatically for different animals, and additional calibration experiments would have been necessary for a different tumour model (using an independent measure such as laser Doppler anemometry). Moreover, it is unlikely that a different choice of animal tumour for these experiments would provide significant improvements over our model, since small macroscopic motions will be a problem for any animal study using such highly motion-sensitive pulse sequences. In general, motion during an imaging sequence that requires more than one excitation for all the phase-encoding steps produces random phase shifts that can add or subtract to the effect of the phase-encoding gradient from line to line in k-space. These can result in severe ghosting artifacts and smearing of the signal intensity in the phase-encode direction. In addition, the use of strong gradients that increase sensitivity to small velocities means that even subtle motions during the scan are an important source of error and image artifacts.

Because macroscopic motions during a scan can often not be avoided, several technical strategies have been developed for overcoming these problems. Two main approaches have been extensively tested and proven effective: motion-correction techniques, and rapid imaging techniques that can acquire an entire image in less than one second (e.g. echo-planar imaging). One motion-correction approach is to use first-order flow-compensation to zero the phase artifacts from linear motion; however, this requires a significant reduction in diffusion-weighting. [78] Another approach is the use of a second, non-phase-encoded "navigator echo" in the PGSE sequence to correct phase errors due to rigid linear and rotational motions. [78,79] The chief limitation of this technique is that it is unable to correct for higher orders of motion, or motion that is spatially varying across the slice. Moreover, it is unlikely that the addition of navigator echoes can fully correct the motions observed during our long exam times. In echo-planar imaging (EPI), the entire set of echoes necessary to form an image can be collected with only a single rf excitation pulse (single-shot EPI). The complete image acquisition normally takes less than 100 ms. For single-shot EPI, image artifacts due to macroscopic motions are completely eliminated. The advent of single-shot, diffusion-weighted EPI has made it possible to obtain quantitative diffusion data *in vivo* from virtually artifact-free images. [80]

Normally, diffusion-weighted EPI is performed with a spin-echo preparation sequence, and a single-shot EPI acquisition. One disadvantage of this approach is that the signal-to-noise in EPI images is generally much less than what can be obtained using a conventional, PGSE sequence, degrading the precision with which the diffusion measurements can be obtained. The addition of diffusion gradients further decreases the signal-to-noise in the images. One possible solution to this problem is to reduce the signal loss due to T_2 relaxation by increasing diffusion gradient amplitudes, and decreasing the echo time, TE. This would result in a substantial increase in initial signal-to-noise at $b = 0$ s/mm^2, allowing high quality images to be obtained for much higher b factors. This approach argues for the use of specialized, high-strength gradient coils to provide these higher gradient amplitudes. As an example, we can consider the benefit of increasing the gradient strength for each coil to 100 mT/m. Applying these gradients along all three axes gives a total gradient strength of 173 mT/m. Using diffusion-pulse timings of $\delta = 5$ ms, $\Delta = 15$ ms, the smallest TE that can be achieved (using the same acquisition parameters as in our study) is TE = 30 ms. For $T_2 = 68$ ms (See Appendix 2), the gain in signal achieved at this TE is approximately 50% over that obtained in our study with TE = 56 ms. Moreover, a maximum diffusion weighting of $b = 717$ s/mm^2 could be obtained using these parameters. A secondary benefit to this approach is the ability to dramatically decrease the T_2-weighting in an image. In PGSE images with significant T_2-

weighting, the image contrast is determined by a mix of ADC- and T_2-weighting. Since the ADC and T_2 reflect different aspects of water mobility within the tissue, these can often have opposing effects on signal intensity within a voxel. Further, if several different T_2 compartments are present within a single voxel, T_2-weighting of these compartments will affect the accuracy of the mean ADC measurement for the voxel.

EPI would enable rapid acquisition of a series of diffusion-weighted images, making it technically possible to obtain an entire diffusion decay curve in less than one minute. This would provide more information about the character of the diffusion decay than a three-point measurement. In addition, the availability of higher-strength gradients would provide stronger diffusion-weighting, and increased precision of the diffusion asymptote measurement. According to prior work by Turner and Le Bihan, [81] the maximum diffusion-weighting in our study (450 s/mm^2) may not be adequate for complete suppression of the microvascular flow component of the signal. In our prior example, where the maximum available gradient strength is increased to 173 mT/m, the diffusion b factor that could be obtained with TE = 30 ms increased dramatically to b = 717 s/mm^2. The availability of higher-strength gradients therefore makes it possible to sample the asymptotic portion of the decay curve, and thereby determine the molecular diffusion coefficient in tissue independent from the microvascular flow.

5:   Development of Hardware for Microvessel/Diffusion Breast Imaging

A high-strength 3-axis local gradient coil set was constructed for magnetic resonance imaging of the breast. This coil design will allow diffusion imaging and high-velocity-resolution blood flow imaging around human breast tumours in clinically acceptable exam times. These are the first specialized gradient coils for breast imaging to ever be presented (2nd Meeting of the Society of Magnetic Resonance, San Francisco, CA, August 1994), and are the first ultra-high-strength gradient coils (>200mT/m) designed for human imaging applications (for body parts larger than fingers). The coils were tested using a grid phantom, and a diffusion phantom, and demonstrated excellent gradient uniformity and accurate diffusion measurement in the region of interest that we defined for breast imaging (based on common bra sizes).

The high gradient efficiencies of these coils will allow much higher spatial-resolution imaging than can currently be achieved in a clinical setting, and additionally, will provide very large amplitude motion-sensitizing gradients, thus facilitating diffusion imaging or flow imaging in small blood vessels while maintaining short echo times. T2 has been measured for human breast tissue, with reported values ranging between 60-150 ms. [82,83] Recently, we reported T2 ~ 70 ms for human breast tumour (MCF7 human breast carcinoma) growing in a mouse mammary fat pad. (Appendix 2) More fibrous tumours can have significantly shorter T2s. For this reason, initial signal loss at b=0 s/mm^2 due to T2-weighting of the image can severely limit the range of b-factors for which images can be obtained, which has the result of limiting the precision of the ADC measurement. Our approach is to shorten TE while maintaining diffusion weighting by increasing diffusion gradient amplitudes. This gives a substantial increase in initial signal intensity for b=0 s/mm^2, allowing high quality images to be obtained for much higher b-factors. Even in cases where signal loss from T2-weighting is not so severe as to limit ADC precision, the ability to obtain high diffusion weighting with short TE reduces dramatically the T2 contrast in an image. This will allow acquisition of a diffusion-weighted image where the contrast is determined mainly by tissue ADC, rather than by a mix of ADC and T2.

Suggestions for Improvements:

Imaging results with these coils demonstrated excellent gradient uniformity for two of three axes in a large region near the top of the coils, and acceptable gradient uniformity for the third (Y)

axis in a smaller region. Initially, the feasibility for using this coil design to measure diffusion and microvessel flow in breast lesions will be evaluated clinically by selecting women who have breast lesions that can be positioned inside our defined volume of interest; however, improvements on the electrical design of the Y gradient coil to provide more uniform gradients over a larger volume would allow scanning with a wider range of breast sizes.

The coils are not torque-balanced, and the horizontal return-wire plates experience strong forces in the upward/downward direction. It is possible to constrain the motion of the coils by an appropriately designed mounting system, but the design of such a system for human imaging is beyond the scope of this thesis, and will not be undertaken immediately. It was therefore decided that no human images would be obtained with the initial prototype coils built for this paper, and that subsequent prototypes would require extensive testing before an attempt to obtain images of a human breast would be made.

This paper (included as Appendix 3) has been published as: C.F. Maier, H.N. Nikolov, K.C. Chu, B.A. Chronik, B.K. Rutt, "Practical Design of a High-Strength Breast Gradient", Magnetic Resonance in Medicine, **39**(3), pp.392-398. Portions of this work have been presented at: the 2nd Meeting of the Society of Magnetic Resonance, San Francisco, CA, August 1994 and the 3rd Meeting of the Society of Magnetic Resonance, Nice, France, August 1995. This work received the University of Western Ontario's Dean's Award for Excellence in Research (1995), and was an invited presentation at the Society of Magnetic Resonance Breast Imaging Workshop, Washington D.C., June 24-25,1995.

6. Conclusions:

1.   The fibroadenomas in our histological study of lesion vascularity contained, on average, more microvessels than some of the invasive carcinomas. This finding directly contradicts the assertion by imaging researchers that benign breast lesions are not vascularized.

2.   The numbers of small vessels were higher around the boundaries of invasive carcinomas compared to the lesion centers, whereas small vessels were more uniformly distributed in fibroadenomas. This characteristic spatial distribution of blood vessels may allow differentiation between fibroadenomas and carcinomas using non-invasive imaging methods sensitized to flow in microvessels.

3.   Quantitative diffusion measurements were performed in MCF7 human breast tumours implanted in nude mice. Apparent Diffusion Coefficients were specific for various components of solid tumours (viable tumour, necrosis, fibrous tissue). Diffusion maps were compared to histology, and correlated well with gross tumour morphology. These measurements provide a foundation for the IVIM experiments that will be undertaken.

4.   PGSE measurements made in a well-vascularized tumour model were highly variable due to macroscopic mouse motions during the course of the MR imaging protocol. The precision of these measurements was insufficient for reliable calculation of vascular parameters using IVIM theory. These results indicate that higher gradient strengths are necessary to perform fast, motion-insensitive diffusion-weighted MR protocols.

5.   An ultra-high-strength 3-axis local gradient coil set was constructed for magnetic resonance imaging of the breast. This coil design will allow diffusion imaging and high-velocity-resolution blood flow imaging around human breast tumours in clinically acceptable exam times. Initial imaging and diffusion measurements using phantoms are promising and prove our design concept; however, construction of further prototypes and more extensive testing is required before human scanning may be safely undertaken.

7. References

1. Schmitt, E. L. and Threatt, B. Characteristics of breast cancer in an incident cancer population. Am.J.Roentgenol. 143:402-406, 1984.
2. Xenophon, L. Imaging techniques for breast disease. Clin.Obstet.Gynaecol. 37 no.4:933-943, 1994.
3. Verbeek, A. L., Hendriks, J. H., Holland, R., Mravunac, M., Sturmans, F. and Day, N. E. Reduction of breast cancer mortality through mass screening with modern mammography: First results of the Nijmegen project, 1975-1981. Lancet 1(1):1222-1224, 1984.
4. Baker, L. H. Breast cancer detection demonstration project: Five-year summary report. CA - A Cancer Journal for Clinicians 32:194-225, 1982.
5. Williams, S. M., Kaplan, P. A., Petersen, J. C. and Lieberman, R. P. Mammography in women under age 30: Is there clinical benefit? Radiology 161:49-51, 1986.
6. Ciatto, S., Cataliotti, L. and Distante, V. Nonpalpable lesions detected with mammography: Review of 512 consecutive cases. Radiology 165:99-102, 1987.
7. Dershaw, D. D., Shank, B. and Reisinger, S. Mammographic findings after breast cancer treatment with local excision and definitive irradiation. Radiology 164:455-461, 1987.
8. Harris, V. J. and Jackson, V. P. Indications for breast imaging in women under age 35 years. Radiology 172:445-448, 1989.
9. Logan-Young, W. W., Janus, J. A., Destounis, S. V. and Yanes Hoffman, N. Appropriate role of core breast biopsy in the management of probably benign lesions. Radiology 190:313-314, 1994.
10. Jackman, R. J., Nowels, K. W., Shepard, M. J., Finkelstein, S. I. and Marzoni, F. A. Stereotaxic large-core needle biopsy of 450 nonpalpable breast lesion with surgical correlation in lesions with cancer or atypical hyperplasia. Radiology 193:91-95, 1994.
11. Liberman, L., Dershaw, D. D., Rosen, P. P., Giess, C. S., Cohen, M. A., Abramson, A. F. and Hann, L. E. Stereotaxic core biopsy of breast carcinoma: Accuracy at predicting invasion. Radiology 194:379-381, 1995.
12. Sullivan, D. C. Needle core biopsy of mammographic lesions. Am.J.Roentgenol. 162:601-608, 1994.
13. Kopans, D. B. Caution on core. Radiology 193:325-328, 1994.
14. Fearon, E. R. and Vogelstein, B. A genetic model for colorectal tumorigenesis. Cell 61:759-767, 1990.
15. Sato, T., Akiyama, F., Sakamoto, G., Kasumi, F. and Nakamura, Y. Accumulation of genetic alterations and progression of primary breast cancer. Cancer Res. 51:5794-5799, 1991.
16. Rosner, B. The role of adjuvant chemotherapy in early node-negative breast cancer. In: Treatment of pre-cancerous lesions and early breast cancer, edited by Arial, I.M. and Cahan, A.C. Baltimore: Williams and Wilkins, 1993.
17. McGuire, W. L., Tandon, A. K., Allred, D. C., Chamness, G. C. and Clark, G. M. How to use prognostic factors in axillary node-negative breast cancer patients. J.Natl.Cancer Inst. 82:1006-1015, 1990.
18. Bader, J., Lippman, M., Swain, S., Danforth, D., MacDonald, H., Gerber, L., Steinber, S., D'Angelo, T. and Campbell, L. Preliminary report on the NCI early breast cancer study: A prospective randomized comparison of lumpectomy and radiation therapy to mastectomy for Stage I and II breast cancer. Int.J.Radiat.Oncol.Biol.Phys. 13 (Suppl):160, 1987.
19. Fisher, B., Redmond, C., Poisson, R., Margolese, R., Wolmark, N., Wickerham, L., Fisher, E., Deutsch, M., Caplan, R., Pilch, Y., Glass, A., Shibata, H., Lerner, H., Terz, J. and

Sidorovich, L. Eight-year results of a randomized clinical trial comparing total mastectomy and lumpectomy with or without irradiation in the treatment of breast cancer. New Engl.J.Med. 320:822-828, 1989.

20. Rosen, P.P. "Intraductal carcinoma" In: Rosen's breast pathology, Philadelphia: Lippincott-Raven, 1997, pp. 227-273.

21. Gasparini, G., Weidner, N. and Bevilacqua, P. Tumor microvessel density, p53 expression, tumor size, and peritumoral lymphatic vessel invasion are relevant prognostic markers in node-negative breast carcinoma. J.Clin.Oncol. 12:454-466, 1994.

22. Mansour, E. G., Ravdin, P. M. and Dressler, L. Prognostic factors in early breast carcinoma. Cancer Suppl. 74 no.1:381-400, 1994.

23. Folkman, J. What is the evidence that tumors are angiogenesis dependent? J.Natl.Cancer Inst. 82 no.1:4-6, 1990.

24. Sutherland, R. M., McCredie, J. A. and Inch, W. R. Growth of multicell spheroids in tissue culture as a model of nodular carcinomas. J.Natl.Cancer Inst. 46:113-120, 1971.

25. Folkman, J. and Hochberg, M. Self-regulation of growth in three dimensions. J.Exp.Med. 138:745-753, 1973.

26. Sutherland, R. M. Cell and environment interactions in tumour microregions: The multicell spheroid model. Science 240:177-184, 1988.

27. Knighton, D., Ausprunk, D., Tapper, D. and Folkman, J. Avascular and vascular phases of tumour growth in the chick embryo. Br.J.Cancer 35:347-356, 1977.

28. Folkman, J., Watson, K., Ingber, D. and Hanahan, D. Induction of angiogenesis during transition from hyperplasia to neoplasia. Nature 339:58-61, 1989.

29. Folkman, J. Angiogenesis and breast cancer. J.Clin.Oncol. 12 no.3:441-443, 1994.

30. Guidi, A. J., Fischer, L., Harris, J. R. and Schnitt, S. J. Microvessel density and distribution in ductal carcinoma in situ of the breast. J.Natl.Cancer Inst. 86 no.8:614-619, 1994.

31. Bose, S., Lesser, M. L., Norton, L. and Rosen, P. P. Immunophenotype of intraductal carcinoma. Arch.Pathol.Lab.Med. 120:81-85, 1996.

32. Brem, S. S., Jensen, H. M. and Gullino, P. M. Angiogenesis as a marker of preneoplastic lesions of the human breast. Cancer 41:239-244, 1978.

33. Chodak, G. W., Haudenschild, C., Gittes, R. F. and Folkman, J. Angiogenic activity as a marker of neoplastic and preneoplastic lesions of the human bladder. Ann.Surg. 192 no.6:762-771, 1980.

34. Jensen, H. M., Chen, I., DeVault, M. R. and Lewis, A. E. Angiogenesis induced by "normal" human breast tissue: A probable marker for precancer. Science 218 no.15:293-295, 1982.

35. Ziche, M. and Gullino, P. M. Angiogenesis and neoplastic progression in vitro. J.Natl.Cancer Inst. 69 no.2:483-487, 1982.

36. Lawson, R. Implications of surface temperatures in the diagnosis of breast cancer. Can.Med.Assoc.J. 75:309-310, 1956.

37. Sterns, E. E., Curtis, A. C., Miller, S. and Hancock, J. R. Thermography in breast diagnosis. Cancer 50:323-325, 1982.

38. Revel, D., Brasch, R. C., Paajenen, H., Rosenau, W., Grodd, W., Engelstad, B., Fox, P. and Winkelhake, J. Gd-DTPA contrast enhancement and tissue differentiation in MRI of experimental breast carcinoma. Radiology 158:319-323, 1986.

39. Heywang, S. H., Wolf, A., Pruss, E., Hilbertz, T., Eiermann, W. and Permanetter, W. MRI of the breast with Gd-DTPA: Use and limitations. Radiology 171:95-103, 1989.

40. Burns, P. N., Halliwell, M., Wells, P. N. and Webb, A. J. Ultrasonic Doppler studies of the breast. Ultrasound Med.Biol. 8:127-143, 1982.

41. Nunes, L. W., Schnall, M. D., Orel, S. G., Hochman, M. G., Langlotz, C. P., Reynolds, C. A. and Torosian, M. H. Breast MR imaging: Interpretation model. Radiology 202:833-841, 1997.

42. Gilles, R., Guinebretiere, J. M. and Lucidarme, O. Nonpalpable breast tumours: Diagnosis with contrast-enhanced subtraction dynamic MR imaging. Radiology 191:625-631, 1994.

43. Weidner, N., Semple, J. P., Welch, W. R. and Folkman, J. Tumor angiogenesis and metastasis: Correlation in invasive breast carcinoma. New Engl.J.Med. 324 no.1:1-7, 1991.

44. Weidner, N., Folkman, J., Pozza, F., Beliacqua, P., Allred, E. N., Moore, D. H., Meli, A. and Gasparini, G. Tumour angiogenesis: A new significant and independent prognostic indicator in early-stage breast carcinoma. J.Natl.Cancer Inst. 84 no.24:1875-1887, 1992.

45. Bosari, S., Lee, A. K. C., DeLellis, R. A., Wiley, B. D., Heatley, G. J. and Silverman, M. L. Microvessel quantitation and prognosis in invasive breast carcinoma. Hum.Pathol. 23:755-761, 1992.

46. Gasparini, G. and Harris, A. L. Clinical importance of the determination of tumor angiogenesis in breast carcinoma: Much more than a new prognostic tool. J.Clin.Oncol. 13 no.3:765-782, 1995.

47. Fox, S. B., Leek, R. D., Smith, K., Hollyer, J., Greenall, M. and Harris, A. L. Tumor angiogenesis in node-negative breast carcinomas: Relationship with epidermal growth factor receptor, estrogen receptor, and survival . Breast Cancer Res.Treat. 29:109-116, 1994.

48. Visscher, D. W., Lawrence, W. D. and Boman, S. Angiogenesis in breast carcinoma -clinicopathologic relevance and patential use as a quantifiable surrogate endpoint biomarker. J.Cell.Biochem.Suppl. 19:146-152, 1994.

49. Guinebretiere, J. M., Le Monique, G., Gavoille, A., Bahi, J. and Weidner, N. Angiogenesis and risk of breast cancer in women with fibrocystic disease. J.Natl.Cancer Inst. 86 no.8:635-636, 1994.

50. Heywang, S. H., Hahn, D., Schmidt, H., Krischke, I., Eiermann, W., Bassermann, R. and Lissner, J. MRI of the breast using Gadolinium-DTPA. J.Comput.Assist.Tomogr. 10(2):199-204, 1986.

51. Kaiser, W. A. and Zeitler, E. MRI of the breast: fast imaging sequences with and without Gd-DTPA: preliminary observations. Radiology 170:681-686, 1989.

52. Pierce, W. B., Harms, S. E., Flamig, D. P., Griffey, R. H., Evans, W. P. and Hagans, J. E. Three-dimensional gadolinium-enhanced MRI of the breast: Pulse sequence with fat suppression and magnetization transfer contrast. Radiology 181:757-763, 1991.

53. Heywang-Kobrunner, S. H. Contrast-enhanced MRI of the breast. Inv.Radiol. 29(1):94-104, 1994.

54. Flickinger, F. W., Allison, J. D., Sherry, R. M. and Wright, J. C. Differentiation of benign from malignant breast masses by time-intensity evaluation of contrast enhanced MRI. Magn.Reson.Imaging 11:617-620, 1993.

55. Gribbestad, I. S., Neilson, G., Fjosne, H., Fougner, R., Haugen, O. A., Petersen, S. B., Rinck, P. A. and Kvinnsland, S. Contrast-enhanced magnetic resonance imaging of the breast. Acta Oncol. 31 no.8:833-842, 1992.

56. Stack, J. P., Redmond, O. M., Codd, M. B., Dervan, P. A. and Ennis, J. T. Breast disease: tissue characterization with Gd-DTPA enhancement profiles. Radiology 174:491-494, 1990.

57. Greenstein-Orel, S., Mendonca, M. H., Reynolds, C., Schnall, M. C., Solin, L. J. and Sullivan, D. C. MR imaging of ductal carcinoma in situ. Radiology 202:413-420, 1997.

58. Le Bihan, D., Breton, E., Lallemand, D., Grenier, P., Cabanis, E. A. and Laval-Jeantet, M. MR imaging of intravoxel incoherent motions: Application to diffusion and perfusion in

neurologic disorders. Radiology 161:401-407, 1986.

59. Dent, D. M. and Cant, P. J. Fibroadenoma. World J.Surg. 13:706-710, 1989.

60. Turner, R., Le Bihan, D. and Chesnick, A. S. Echo-planar imaging of diffusion and perfusion. Magn. Reson. Med 247:253, 1991.

61. Le Bihan, D., Moonen, C. T., van Zijl, P. C., Pekar, J. and DesPres, D. Measuring random microscopic motion of water in tissues with MRI: A cat brain study. J. Comput. Assist. Tomogr. 15(1):19-25, 1991.

62. Chenevert, T., Pipe, J. G., Williams, D. M. and Brunberg, J. A. Quantitative measurement of tissue perfusion and diffusion in Vivo. Magn. Reson. Med 17:197-212, 1991.

63. Lorenz, C. H., Pickens, D. R., Puffer, D. B. and Price, R. R. Magnetic resonance diffusion/perfusion phantom experiments. Magn. Reson. Med 19:254-260, 1991.

64. Neil, J. J., Scherrer, L. A. and Ackerman, J. J. An approach to solving the dynamic range problem in measurement of the pseudodiffusion coefficient in Vivo with spin echoes. J. Magn. Reson. 95:607-614, 1991.

65. Neil, J. J., Bosch, C. S. and Ackerman, J. J. An evaluation of the sensitivity of the IVIM method of blood flow measurement to changes in cerebral blood flow. Magn. Reson. Med 32:60-65, 1994.

66. King, M. D., van Bruggen, N., Busza, A. L., Houseman, J., Williams, S. R. and Gadian, D. G. Perfusion and diffusion MR imaging. *Magn. Reson. Med* 24:288-301, 1992.

67. MacFall, J. R., Maki, J. H., Johnson, G. A., Hedlund, L., Benveniste, H. and Copher, G. Diffusion/microcirculation MRI in the rat brain. Magn. Reson. Med 19:305-310, 1991.

68. Pekar, J., Moonen, C. T. and van Zijl, P. C. On the precision of diffusion/perfusion imaging by gradient sensitization. Magn. Reson. Med 23:122-129, 1992.

69. Kwong, K. K., McKinstry, R. C., Chien, D., Crawley, A. P., Pearlman, J. D. and Rosen, B. R. CSF-suppressed quantitative single-shot diffusion imaging. *Magn. Reson. Med* 21:157-163, 1991.

70. Henkelman, R. M., Neil, J. J. and Xiang, Q. S. A quantitative interpretation of IVIM measurements of vascular perfusion in the rat brain. Magn. Reson. Med 32:464-469, 1994.

71. Kennan, R. P., Gao, J. H., Zhong, J. and Gore, J. C. A general model of microcirculatory blood flow effects in gradient sensitized MRI. Med. Phys. 21(4):539-545, 1994.

72. Neeman, M., Freyer, J. P. and Sillerud, L. O. A simple method for obtaining cross-term-free images for diffusion anisotropy studies in NMR microimaging. Magn. Reson. Med 21:138-143, 1991.

73. Eis, M. and Hoehn-Berlage, M. Correction of gradient crosstalk and optimization of measurement parameters in diffusion MR imaging. J. Magn. Reson. 107:222-234, 1995.

74. Conturo, T. E., McKinstry, R. C., Akbudak, E. and Robinson, B. H. Encoding of anisotropic diffusion with tetrahedral gradients: A general mathematical diffusion formalism and experimental results. Magn. Reson. Med 35:399-412, 1996.

75. Fidler, I. J. Selection of successive tumour lines for metastasis. Nature Med. Biol. 242:148-149, 1973.

76. Zhao, M., Fortan, L. G. and Evelhoch, J. L. The effects of isofluorane and halothane on blood flow and 31P NMR spectra in murine RIF-1 tumours. Magn. Reson. Med 33:610-618, 1995.

77. Simpson, J. H. and Carr, H. Y. Diffusion and nuclear spin relaxation in water. Phys. Rev. 111(5):1201-1202, 1958.

78. Johnson, G. A. and Maki, J. H. In vivo measurement of proton diffusion in the presence of coherent motion. Invest. Radiol. 26:540-545, 1991.

79. Ordidge, R. J., Helpern, J. A., Qing, Z. X., Knight, R. A. and Nagesh, V. Correction of

motional artifacts in diffusion-weighted MR images using navigator echoes. Magn. Reson. Imag. 12:455-460, 1994.

81. Turner, R. and Le Bihan, D. Single-shot diffusion imaging at 2.0 Tesla. J. Magn. Reson. 86:445-450.

82. Chu, D. Z., Yamanashi, W. S., Frazer, J., Hazlewood, C. F., Gallager, H. S., Boddie, A. W. and Martin, R. G. Proton NMR of human breast tumors: correlation with prognostic parameters. J. of Surg.Onc. 36:1-4, 1987.

83. Graham, S. J., Bronskill, M. J., Byng, J. W., Yaffe, M. J. and Boyd, N. F. Quantitative correlation of breast tissue parameters using MR and X-ray mammography. Br.J.Cancer 73:162-168, 1996.

RF

time

Slice
Select
Gradient

Diffusion
Encoding
Gradient

g

Phase
Encoding
Gradient

Frequency
Encoding
Gradient
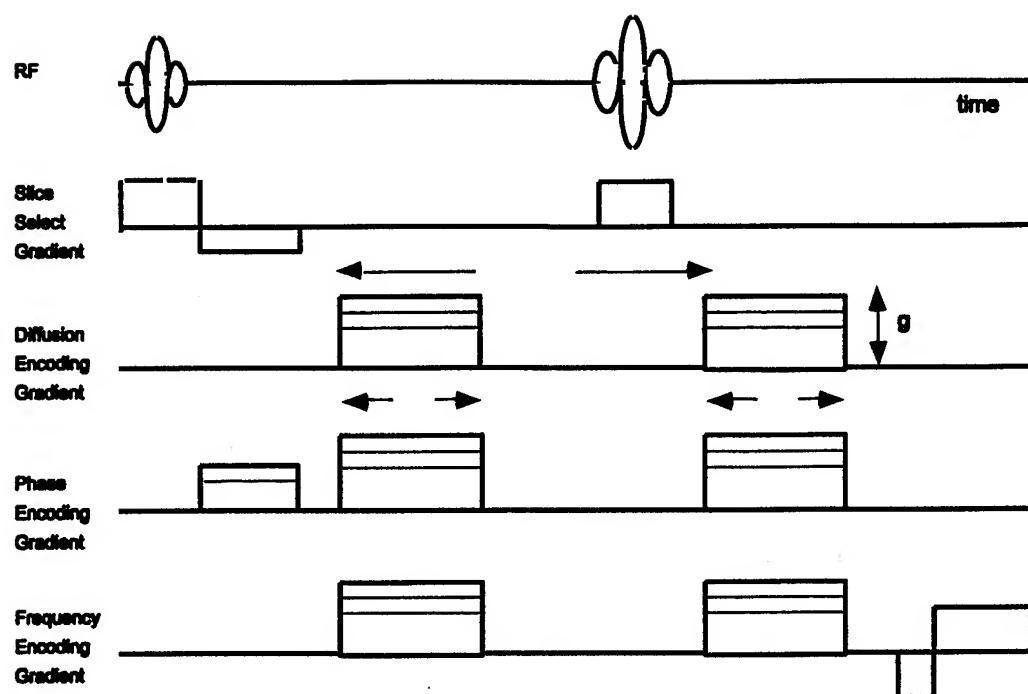
Figure 1. PGSE pulse sequence for diffusion/IVIM measurements with TE=75ms, δ=10ms, and Δ=50ms. b-factors for this TE range between 0 and 485 s/mm2.

x 10⁴ Signal Intensity Timecourse in a Water Standard
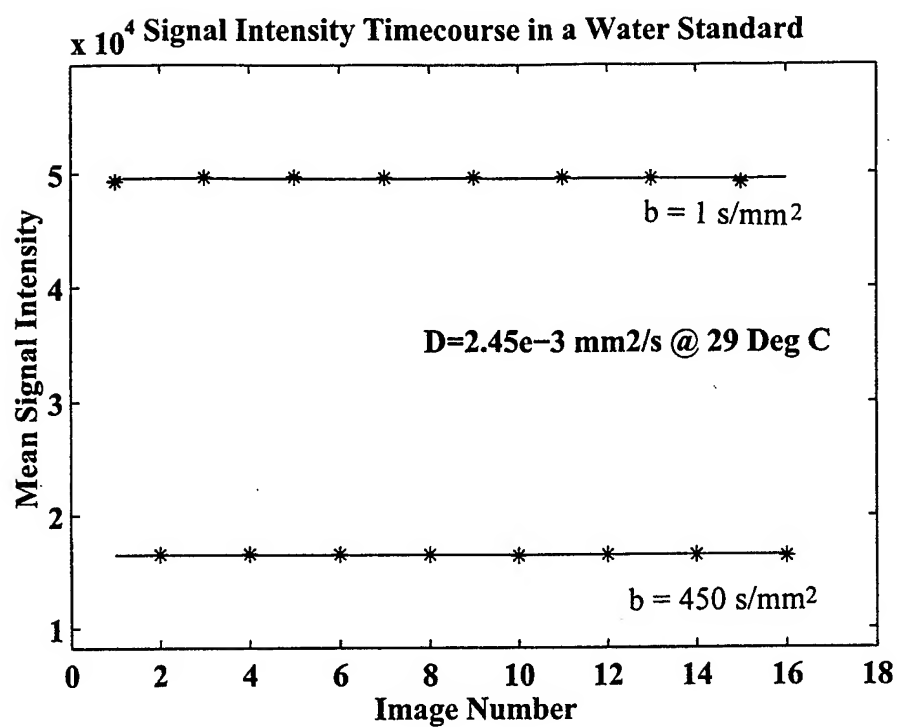
Figure 2. Mean signal intensity inside an ROI defined within a water standard. The acquisition time for each image was 4.5 min.
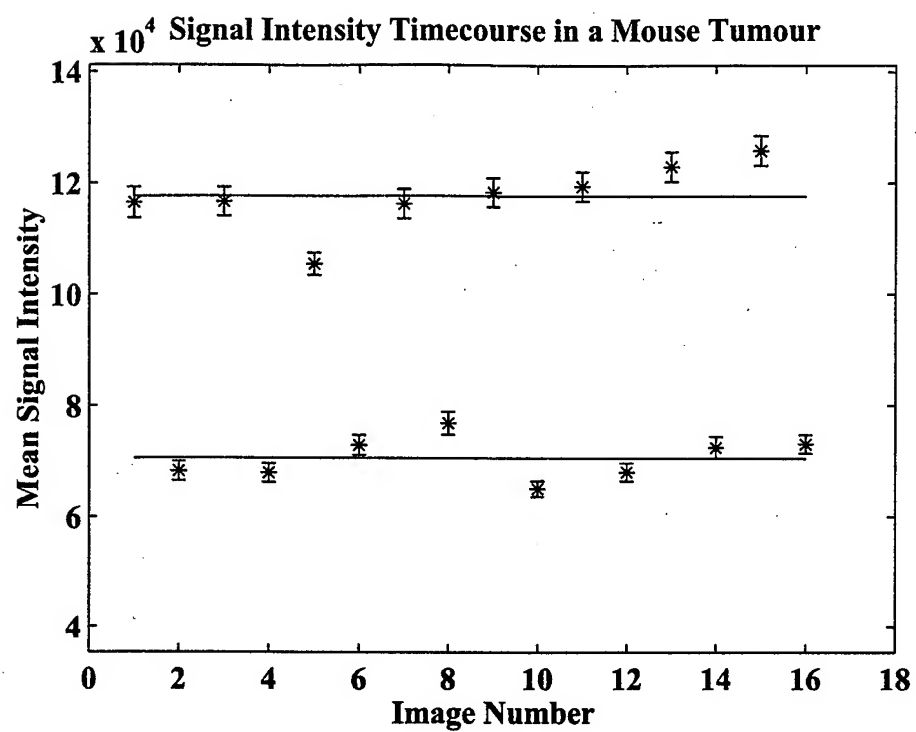
Figure 3. Mean signal intensity inside an ROI defined for a mouse tumour. The acquisition time for each image was 4.5 min.

Appendix 1

Kirsten L. Weind, BSc
Cynthia F. Maier, PhD
Brian K. Rutt, PhD
Madeleine Moussa, MD

Author contributions:
Guarantor of integrity of entire study,
C.F.M.; study concepts and design,
K.L.W., C.F.M., B.K.R., M.M.; definition
of intellectual content, K.L.W., C.F.M.;
literature research, K.L.W., C.F.M.; data
acquisition, M.M.; data analysis, K.L.W.,
C.F.M.; statistical analysis, K.L.W.;
manuscript preparation, K.L.W., C.F.M.;
manuscript editing and review, K.L.W.,
C.F.M., B.K.R., M.M.

Invasive Carcinomas and Fibroadenomas of the Breast: Comparison of Microvessel Distributions—Implications for Imaging Modalities[1]

PURPOSE: To compare spatial patterns of blood vessels between invasive breast carcinomas and fibroadenomas to improve the diagnostic specificity of noninvasive vascular magnetic resonance imaging and color Doppler ultrasound.

MATERIALS AND METHODS: Nineteen invasive ductal carcinomas and 20 fibroad-enomas from 39 patients were stained for factor VIII–related antigen. Vessels smaller than 40 μm were counted in ×200 fields defined in peripheral and central areas of the tumor and in normal tissue adjacent to fibroadenomas. Significant differences in vessel density were determined with Student t tests and one-way analyses of variance. Distributions of vessels 40 μm or larger were qualitatively evaluated.

RESULTS: There were 9–105 vessels (mean, 31.4 vessels) smaller than 40 μm per ×200 peripheral and 4–57 vessels (mean, 20.1 vessels) smaller than 40 μm per ×200 central carcinoma field. There was no significant difference in vessel density between the two groups. Peripheral microvessel density was significantly higher ($P < .01$) than central microvessel density in 15 (79%) of the 19 carcinomas and in three (16%) of 19 fibroadenomas. (A Student t test could not be performed in one case of fibroadenoma; size permitted only one countable field according to the authors' criteria.) The 18 cases with normal tissue had 21–229 vessels (mean, 80.5 vessels) per field; in 16 (89%) of the 18 cases, these vessel counts were significantly higher ($P < .01$) than those in the fibroadenoma cases. Vessels 40 μm or larger were found mainly in the periphery of carcinomas and were more uniformly distributed in fibroadenomas.

CONCLUSION: Evaluation of the spatial distribution of vessels and the ability to resolve vessel sizes may add valuable information to the imaging-based diagnostic work-up of indeterminate solid breast lesions.

At present, the primary method of the detection and diagnosis of breast disease is conventional mammography, which has a proved sensitivity of 85%–95% (1,2). However, specificity with this modality is substantially lower, and additional diagnostic procedures are often necessary (3,4). A definitive diagnosis is sometimes possible with noninvasive techniques, but, for most lesions, biopsy is necessary to obtain reliable results (5–8). In the majority of cases, breast lesions progressing to biopsy are benign (3,9,10). Surgical biopsy in these cases has served only to provide a diagnosis, since it is not necessary to remove a benign lesion unless it is causing pain (11,12). This has led to the evaluation of imaging methods such as magnetic resonance (MR) imaging and color Doppler ultrasound (US) as adjunctive noninvasive diagnostic examinations (13,14).

Both these modalities rely on the principle that an increase in the number of blood vessels, increased vascular permeability, or both around malignant lesions result from tumor angiogenesis and create characteristic, identifiable patterns that can be distin-guished from those associated with benign lesions. Although early contrast material–enhanced MR imaging and color Doppler US studies were reported to have extremely high

477

Case No./ Patient Age (y)	Tumor Diameter (cm)	Tumor Grade	Lymph Node Status	Vessel Count per Field				Ratio of Mean in Periphery to Mean in Center
				Mean ± Standard Deviation		Range		
				Periphery	Center	Periphery	Center	
1/44	1.5	II	Negative	13.0 ± 2.20	8.00 ± 2.20	9–16	5–12	1.63
2/66	0.7	II	Negative	20.8 ± 4.40	11.4 ± 2.10	16–26	9–14	1.82
3/74	2.0	I	Not known	25.1 ± 6.80	17.3 ± 3.70	17–38	13–23	1.45
4/47	1.7	II	Positive	32.0 ± 10.5	15.6 ± 5.50	20–53	8–25	2.05
5/75	3.0	II	Not known	19.8 ± 3.20	10.8 ± 2.40	16–24	7–15	1.83
6/70	2.5	III	Positive	19.8 ± 2.40	7.70 ± 1.80	16–22	5–10	2.57
7/54	2.5	II	Positive	24.5 ± 4.40	10.8 ± 4.70	17–30	4–17	2.27
8/55	1.5	II	Negative	29.1 ± 10.3	28.8 ± 4.30	14–49	23–35	1.01
9/49	2.2	III	Positive	29.0 ± 3.30	21.1 ± 7.00	25–32	14–32	1.37
10/30	1.8	III	Positive	71.0 ± 18.1	33.9 ± 10.8	54–105	24–57	2.09
11/80	2.5	III	Not known	30.2 ± 6.60	16.6 ± 3.20	22–43	13–23	1.82
12/31	2.0	III	Positive	23.4 ± 4.60	18.0 ± 4.90	16–30	10–27	1.30
13/52	1.3	II	Negative	35.4 ± 13.0	17.2 ± 3.90	17–55	9–22	2.06
14/57	1.0	I	Negative	21.6 ± 5.60	22.8 ± 4.30	16–31	18–29	0.95
15/79	2.0	I	Not known	41.6 ± 7.50	35.6 ± 9.50	28–54	24–51	1.17
16/46	5.0	II	Positive	23.6 ± 3.00	19.7 ± 2.60	17–27	16–24	1.20
17/49	2.5	II	Negative	30.1 ± 7.60	18.2 ± 3.30	20–45	13–22	1.65
18/47	1.5	I	Negative	52.5 ± 14.9	42.5 ± 6.30	39–88	36–57	1.24
19/61	0.4	II	Not known	55.1 ± 12.8	25.9 ± 6.40	35–72	18–40	2.13

diagnostic specificity (15–17), further studies with larger sample sizes did not achieve the same accurate delineation of breast carcinomas. In particular, a substantial fraction of fibroadenomas were indistinguishable from malignant lesions (13,18–20). The inability to accurately identify fibroadenomas is a considerable flaw for a potential adjunctive modality, because these lesions often resemble solid carcinomas at both mammography and clinical presentation (21,22) and account for 30%–50% of biopsies of benign lesions (23).

Recently, several MR groups have observed a pattern of heightened contrast material enhancement around the periphery of a lesion in 15%–30% of malignant lesions (24,25). This "positive rim sign" (18) has also been observed by using color Doppler US. It has been suggested that this criterion could aid in separating malignant from benign lesions.

Several researchers (25–27) have also compared MR contrast material enhancement parameters with numbers of blood vessels observed at histologic analysis. In these studies, vessels were counted in areas of highest vascularity or "hot spots," potentially valuable prognostic indicators for invasive carcinomas (28). Two of the three researchers (25,26) found a statistically significant correlation between the degree of enhancement and microvessel density in hot spots. Unfortunately, researchers in none of these studies attempted to evaluate the spatial distribution of vascularity over entire lesions. In addition, no data are available on the

comparison of color Doppler results with histologic confirmation of the presence of larger vessels.

To use vascular imaging techniques effectively, it is necessary to first identify a difference in the vascular pattern between malignant and benign lesions that is prominent enough to allow differentiation of these lesions. In addition, the study of the differences, similarities, or both between vascular distribution and density in malignant and benign breast lesions could serve to illuminate the unique mechanisms contributing to the formation of a microcirculatory network in a malignant tumor and its subsequent role in tumor metastasis. With these objectives in mind, we have evaluated spatial patterns of blood vessel distribution and quantitatively assessed microvessel density in invasive ductal carcinomas and fibroadenomas.

MATERIALS AND METHODS

Routinely processed, formalin-fixed, paraffin-embedded tissue from 39 lumpectomies in 19 patients with 19 invasive ductal carcinomas and in 20 patients with 20 fibroadenomas was retrieved from the files of the Department of Pathology at London Health Sciences Centre, London, Ontario, Canada. Patients with carcinoma ranged in age from 30 to 80 years and patients with fibroadenomas ranged in age from 19 to 49 years. Immunohistochemical studies to detect factor VIII-

related antigen (rabbit polyclonal antibody; Dimension Labs, Mississauga, Ontario, Canada; 1:100 dilution) were performed on 4 μm-thick recut sections by using the avidin-biotin peroxidase technique. All tissues were counterstained with hematoxylin. A standard hematoxylin-eosin slide was also prepared from an adjacent slice of the fibroadenomas for classification purposes.

Fibroadenomas were classified by one of the investigators (M.M.) by using the three categories defined by Ohtani and Sasano (29)—myxoid, fibrocellular, and sclerosed—with the addition of two categories: mixed lesions containing both myxoid and fibrous characteristics (fibromyxoid) and lesions showing only cellular characteristics (cellular). Patient age, tumor diameter, tumor grade (Scarff-Bloom-Richardson criteria) (30), and lymph node status were obtained from the surgical pathology consultation report.

To evaluate the spatial distribution of capillaries and smaller arterioles and venules, microvessels smaller than 40 μm in diameter (31) were counted by using light microscopy on ×200 fields (×20 objective lens, ×10 ocular lens) by one of the investigators (M.M.). Vessel identification was performed according to the criteria used by Weidner et al (28). Any brown-staining, freestanding endothelial cell or group of endothelial cells was counted as a vessel.

Ten fields were chosen at random in both the central and peripheral regions of each tumor (provided there was sufficient

TABLE 2
Fibroadenomas: Clinical Data and Vessel Counts

Case No./ Patient Age (y)	Tumor Diameter (cm)	Tumor Classification	Vessel Count per Field						Ratio of Mean in Periphery to Mean in Center
			Mean ± Standard Deviation			Range			
			Periphery	Center	Normal	Periphery	Center	Normal	
20/41	1.0	Fibromyxoid	34.9 ± 13.2	25.3 ± 5.68	43.6 ± 9.02	15–57	17–35	32–55	1.42
21/47	1.4	Fibromyxoid	33.1 ± 7.34	36.7 ± 10.0	79.6 ± 16.5	24–44	19–58	54–92	0.9
22/43	1.0	Cellular	112 ± 29.8	95.6 ± 24.4	133 ± 58.2	54–157	76–137	75–200	1.17
23/19	3.5	Cellular	35.2 ± 11.9	17.0 ± 4.81	55.0 ± 6.82	20–57	7–25	43–60	2.07
24/44	1.0	Fibrocellular	48.5 ± 13.0	53.4 ± 10.4	75.6 ± 13.3	29–68	40–67	60–96	0.91
25/27	0.6	Sclerosed	47.9 ± 9.75	40.8 ± 5.26	46.8 ± 5.93	31–65	32–46	37–52	1.17
26/38	0.6	Myxoid	51.7 ± 9.04	68.0 ± 19.8	98.2 ± 32.1	41–70	54–82	65–151	0.76
27/43	2.0	Cellular	39.3 ± 13.1	45.7 ± 12.6	110 ± 26.2	20–60	25–71	85–144	0.86
28/31	1.5	Sclerosed	39.1 ± 7.23	27.3 ± 8.96	75.7 ± 16.6	26–47	14–39	57–89	1.43
29/39	2.5	Fibrocellular	29.1 ± 11.0	18.0 ± 6.02	39.6 ± 8.85	15–50	7–27	28–51	1.62
30/49	1.0	Myxoid	40.4 ± 11.0	24.0 ± 9.90	99.2 ± 58.5	27–58	17–31	39–167	1.68
31/22	2.7	Cellular	24.7 ± 6.93	15.0 ± 0.0	53.2 ± 37.2	14–34	15	21–113	1.64
32/34	1.7	Fibromyxoid	30.7 ± 15.8	34.4 ± 12.3	59.2 ± 12.0	14–59	11–51	45–71	0.89
33/35	2.0	Sclerosed	37.4 ± 8.28	30.6 ± 14.1	0	22–50	15–58	0	1.22
34/21	1.1	Fibromyxoid	64.9 ± 12.0	64.6 ± 12.2	0	47–78	46–88	0	1.0
35/27	1.4	Myxoid	51.2 ± 8.89	45.8 ± 10.4	100 ± 49.2	41–65	29–63	54–152	1.12
36/37	1.2	Myxoid	50.8 ± 14.9	52.6 ± 11.5	50.5 ± 24.8	33–77	34–71	33–68	0.97
37/20	2.5	Fibromyxoid	37.0 ± 9.57	21.8 ± 8.47	96.8 ± 25.0	23–55	11–40	66–130	1.7
38/37	1.2	Myxoid	46.0 ± 18.0	30.8 ± 6.58	86.8 ± 19.8	23–75	19–38	55–102	1.49
39/47	1.2	Myxoid	65.0 ± 14.4	66.2 ± 13.9	146 ± 77.9	48–90	48–81	66–229	0.98

tissue). A peripheral field was defined as a field inside the tumor boundary (ie, an imaginary line connecting the most peripheral nests was considered the leading edge of invading cells in the case of invasive carcinomas) with the microscopic field circumference touching the boundary. A central field was defined as a microscopic field inside the tumor at least one ×200 field of view away from the boundary. Central fields were not defined in necrotic, avascular regions of the carcinomas; however, tumors containing necrosis were noted. For fibroadenomas, up to five fields of normal tissue adjacent to the lesion were also evaluated (provided there was sufficient normal tissue within the slide limits).

No tissue present on a carcinoma slide, regardless of histologic appearance, was considered normal (normal-appearing lobules from cancerous breasts have shown an angiogenic up-regulation when compared with lobules from noncancerous breasts [32]). Microvessels 40 μm or larger in diameter were also qualitatively evaluated on each slide.

Student t tests were performed for individual lesions to determine whether there was a statistically significant difference between the vessel density in the periphery and that in the lesion center. (A Student t test could not be performed on one fibroadenoma [case 31]; size permitted only one countable central field according to our criteria.) Ratios of mean peripheral to mean central vessel counts

were calculated for each lesion, and t tests were performed to assess differences in vessel counts or in this ratio between invasive carcinomas and fibroadenomas and between carcinomas with lymph node involvement and carcinomas without lymph node involvement. One-way analyses of variance were performed to evaluate differences in vessel counts between the five categories of fibroadenomas and also between the three grades of invasive carcinomas (Scarff-Bloom-Richardson criteria [30]). In all cases, a significant difference was defined at P less than .01.

RESULTS

Mean vessel counts (vessel density within a ×200 field) and their standard deviations and ranges are shown in Tables 1 and 2 for invasive ductal carcinomas and fibroadenomas, respectively. Invasive ductal carcinomas ranged in diameter from 0.4 to 5.0 cm, while fibroadenomas ranged in diameter from 0.6 to 3.5 cm. The invasive ductal carcinomas could be categorized as follows: four (21%) grade I carcinomas, two without lymph node involvement and two in which no lymph node dissection was performed; 10 (53%) grade II carcinomas, five without lymph node involvement, three with lymph node involvement, and two in which no lymph node dissection was performed; and five (26%) grade III carcinomas, all with lymph node involvement. Classi-

fication of the fibroadenomas yielded six (30%) myxoid, five (25%) fibromyxoid, four (20%) cellular, two (10%) fibrocellular, and three (15%) sclerosed lesions. Large necrotic centers (ie, >30%–40% of the lesion was necrotic) were evident in two (10%) of 19 carcinomas (cases 7 and 10). In one of these tumors (case 10), the area of necrosis was surrounded by a prominent ring of small blood vessels. Smaller areas of partial necrosis (approximately 10%–15% of the lesion was necrotic) were observed within the lesion center in an additional eight (42%) of the 19 invasive ductal carcinomas.

The number of vessels in a ×200 field for the invasive ductal carcinomas ranged between 9 and 105 (mean, 31.4) for the peripheral and 4 and 57 (mean, 20.1) for the central fields. In previous vessel density studies, only areas of highest vascularization within the tumor (tumor hot spots) were selected for vessel counting (28,33,34). Maximum vessel counts for invasive ductal carcinomas in our study were within these reported ranges. For fibroadenomas, the range of vessel densities for the peripheral fields was 14–157 vessels (mean, 46.0 vessels) and that for the central fields was 7–137 vessels (mean, 40.7 vessels). Normal tissue surrounding the fibroadenomas (present in 18 of the 20 cases) had a range of 21–229 vessels (mean, 80.5 vessels) per field. In 16 (89%) of the 18 cases, vessel counts in normal tissue were significantly higher than those in fibroadenomas. It is interesting to note

that the highest normal tissue vessel counts were found in three women aged 43–49 years, while the mean age of patients with fibroadenomas was 35 years. For these three women, the normal breast tissue was noticeably more vascular than that in other patients and was predominantly composed of dense lobular and ductal tissue, with little fatty tissue present.

Vessel counts for invasive ductal carcinomas are shown in Figure 1a; those for fibroadenomas are shown in Figure 1b (cases have been arranged on the x axis in order of increasing tumor diameter). Microvessel density was significantly higher (P < .01) in the tumor periphery than it was in the tumor center in 15 (79%) of the 19 invasive ductal carcinomas and in three (16%) of 19 fibroadenomas.

Figure 2 shows high magnification fields in the periphery (Fig 2a) and center (Fig 2b) of a typical invasive ductal carcinoma (case 13). In one of the four carcinomas in which no significant difference was found between peripheral and central vessel densities (case 18), the carcinoma consisted of many nests of carcinoma cells with distinctive rings of small vessels surrounding each of the nests. The mean ratio of peripheral to central vessel counts was 1.66 ± 0.46 (standard deviation; range, 0.95–2.57) and 1.25 ± 0.36 (range, 0.76–2.07) in invasive ductal carcinomas and fibroadenomas, respectively, and the ratios of peripheral to central vessel counts was significantly different between these groups (P < .01).

The individual peripheral versus central vessel density ratios for both groups of lesions are compared in Figure 3. No correlation was observed between mean peripheral counts, mean central counts, maximum peripheral counts, maximum central counts, or in the peripheral versus central vessel density ratios with carcinoma grade or lymph node status.

One-way analyses of variance performed between the maximum peripheral, maximum central, mean peripheral, and mean central counts of the fibroadenomas yielded no statistically significant difference (P < .01) in vessel densities between the five classifications. All three sclerosed fibroadenomas in our study had numerous blood vessels, comparable even to the number of vessels observed for the cellular and myxoid groups. An example of a sclerosed but highly vascularized fibroadenoma (case 28) is shown in Figure 4, and a typical cellular fibroadenoma (case 22) is shown in Figure 5 for comparison. There was also no correlation of any vascular param-
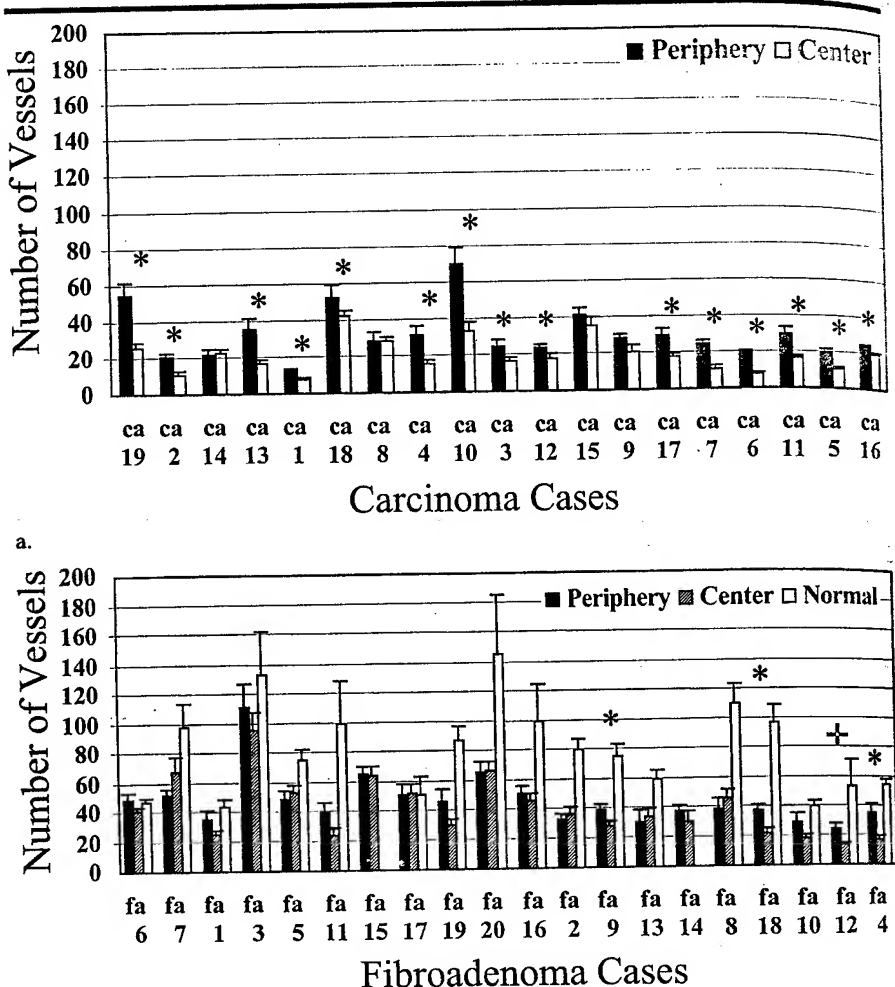

a.

b.

Figure 1. Mean vessel counts of lesions arranged in order of increasing tumor diameter. * = those cases in which the vessel density in the periphery was significantly greater than that in the center (P < .01). (a) Graph shows mean vessel counts in the peripheral and central fields of invasive ductal carcinomas (ca). (b) Graph shows mean vessel counts in the peripheral and central fields of fibroadenomas (fa) and mean vessel counts in the surrounding normal tissue. + = the fibroadenoma case in which only one central field was present and no statistical analysis could be performed. Fibroadenoma cases 1–20 correlate with cases 20–39 in Table 2 (eg, fa 1 = case 20 in Table 2, fa 2 = case 21).

eters with patient age or tumor size for either fibroadenomas or carcinomas.

In eight (42%) of the 19 invasive ductal carcinomas, vessels 40 μm or larger in diameter were observed just outside the leading edge of the tumor (Fig 6). In four (21%) of these cases, larger vessels could also be seen immediately inside the invading boundary. In five additional carcinomas (26%), a patch of larger vessels was observed within a peripheral field of a tumor. Larger vessels were not observed within the centers of any of the carcinomas in our study. In 10 (50%) of the 20 fibroadenomas, the presence of larger vessels was also noted. In six of these cases (30%), there were several large vessels present in the periphery of the lesion;

while in two cases (10%), larger vessels in the periphery were abundant. In the remaining two fibroadenomas (10%), many large vessels were uniformly distributed throughout the lesion. These vessels were easily observed with low magnification.

DISCUSSION

We identified statistically significant overlap in microvessel counts between the invasive ductal carcinomas and fibroadenomas in our study. This finding may help explain the overlap in enhancement characteristics between invasive breast carcinomas and some fibroadenomas on contrast-enhanced MR imaging studies.
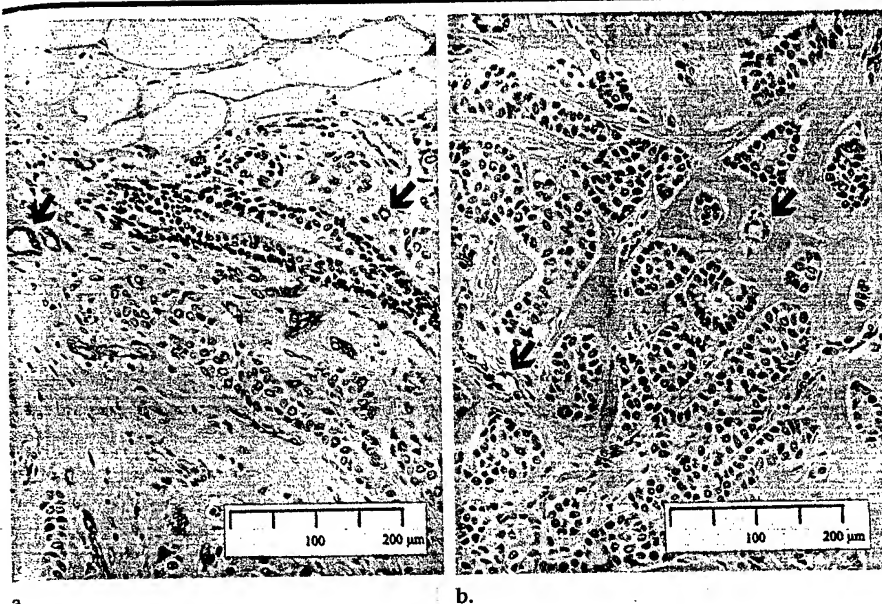
Weind et al

Figure 2. Case 13. Typical invasive ductal carcinoma. (a, b) Pathologic slices show carcinoma in the (a) periphery and (b) center. (Stained for factor VIII–related antigen and counterstained with hematoxylin; original magnification, ×200.) In a and b, arrows show vessels outlined in brown (factor VIII–related antigen causes endothelial cells that line the lumen of the blood vessels to stain brown).
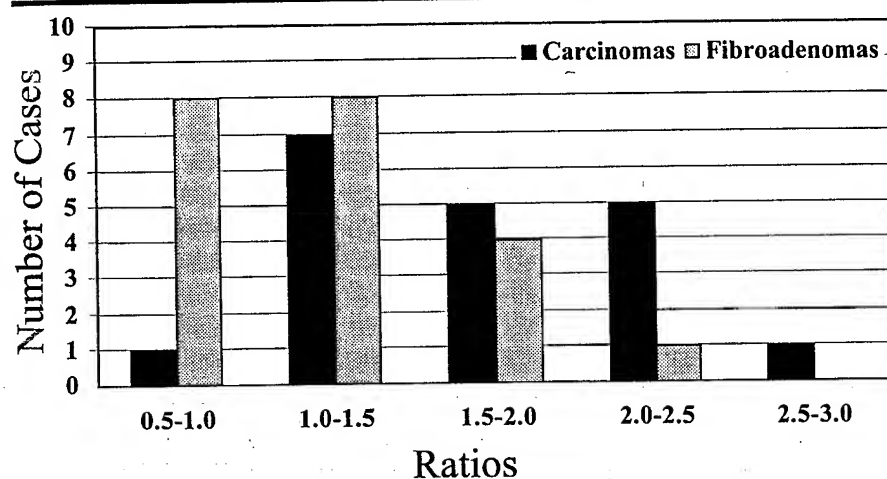

Figure 3. Histogram shows the distribution of mean peripheral versus mean central vessel count ratios for invasive ductal carcinomas and fibroadenomas.

within the same breast can induce new blood vessel formation in a rabbit corneal model (32,36). Therefore, it is not unrealistic to suggest that other benign breast diseases may also achieve an angiogenic state.

Our results support the observation that microvessel density is higher in the active tumor periphery of invasive ductal carcinomas than in the tumor center. These findings are consistent with contrast-enhanced MR imaging findings of rim enhancement in carcinomas. In the study by Buadu et al (25), rim-enhancing carcinomas were observed to have varying degrees of central desmoplasia, associated with lower vessel density. In the work of Orel et al (24), rim enhancement was observed in five of 16 carcinomas, but none of the rim-enhancing carcinomas exhibited central necrosis.

In our group of lesions, a significantly higher microvessel density was observed in the lesion periphery in 15 (79%) of the 19 invasive ductal carcinomas. Only two of these cases (cases 7 and 10) had well-defined necrotic cores, and, moreover, central fields were not defined within these avascular regions; rather, they were limited to areas of viable tumor. An additional eight cases had small necrotic regions within the tumor; however, only five of these had significantly higher peripheral vessel counts than central vessel counts. Although the mean microvessel density was significantly higher in peripheral fields than in central fields in most carcinomas in our sample, there was still considerable overlap between peripheral field counts and central field counts within each lesion. This may explain why the percentage of carcinomas reported to exhibit rim enhancement on MR images is much smaller than the percentage of lesions we found to have increased peripheral vessel density (24,25).

Vessel density in fibroadenomas was more uniform throughout the tumor than it was in carcinomas, with no statistically significant difference between periphery and center in 16 (84%) of 19 cases. Areas of increased vessel density did exist within fibroadenomas; however, these areas usually corresponded to a single or several lobules, within which a uniformly elevated distribution of blood vessels was observed. These results are in accord with the homogeneous MR imaging contrast-enhancement patterns observed for fibroadenomas and are suggestive of possible improvements in specificity that may result from the addition of the evaluation of morphologic features to an MR imaging examination (25,37,38).

Enhancement characteristics on a contrast-enhanced MR image reflect blood volume (microvessel density), blood flow, and vessel permeability, which are all vasculature characteristics that have been linked to tumor angiogenesis. The observed overlap in MR imaging enhancement curves and in microvessel density between carcinomas and fibroadenomas implies that the same processes may be controlling the vascular development in both of these classes of lesions.

It is possible that the numerous small vessels we observed in fibroadenomas may be the result of angiogenic stimulation initiated by the fibroadenoma. This hypothesis is also supported by the increased number of vessels 40 μm or larger observed in the periphery of the fibroadenomas, similar to the pattern of peripheral blood vessels known to be associated with angiogenesis in carcinomas (35). It is well known that premalignant lesions can induce angiogenesis, and it has been shown that benign breast tissue removed from a location distal to a carcinoma but

Two authors (24,39) have compared contrast-enhancement characteristics with histologic findings in an attempt to explain the rapid, marked contrast material enhancement observed in some fibroadenomas. In these studies (24,39), nonsclerosed fibroadenomas enhanced strongly, but the enhancement of sclerosed fibroadenomas was highly variable, with some sclerotic lesions also exhibiting statistically significant rapid signal intensity increases. This finding was contrary to the expectation that sclerotic lesions, being acellular, would have fewer blood vessels than myxoid or cellular lesions. In the group of fibroadenomas in our study, no statistically significant decrease in the number of microvessels was observed in the three sclerotic lesions as compared to the number of microvessels in the cellular or myxoid category. Lesions in all these groups contained areas of low microvessel density and areas of high microvessel density, with no general trend observable with category; however, the number of fibroadenomas in each of our categories was small, and further investigation is required before any definite conclusions can be drawn.

Our observation of larger microvessels in the periphery of both carcinomas and fibroadenomas is consistent with the color Doppler US study by Kubek et al (18), in which a preponderance of detected blood flow near the peripheries of both malignant lesions and fibroadenomas was reported. This finding is not inconsistent with the fact that MR imaging rim enhancement is observed only in malignant lesions, since color Doppler US is sensitive to much larger vessels than is contrast-enhanced MR imaging, and our findings show that the spatial distribution of these larger vessels is different from that of smaller vessels. Two investigators (18,19) have reported that the number of vessels observed by using color Doppler US in fibroadenomas is increased with increasing lesion size. We have not noted any correlation between the number of vessels 40 μm or larger and fibroadenoma size. Very few vessels larger than 200 μm could be observed on a single slide; it was therefore not possible to conclude anything about the spatial distributions of Doppler-detectable vessels in our study.

Numerous investigators have established microvessel density in hot spots as an important prognostic indicator in breast carcinoma (28,40). Several authors have compared MR contrast-enhancement patterns with vessel density in hot spots; these investigations have been more directly relevant to assessing the
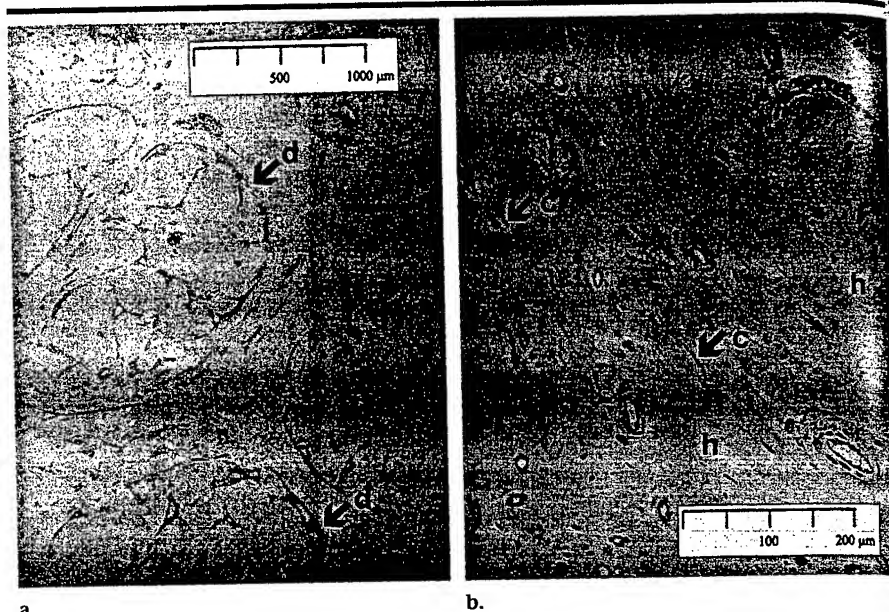

a.   b.

Figure 4. Case 28. Pathologic slices show a sclerosed but highly vascularized fibroadenoma stained for factor VIII–related antigen and counterstained with hematoxylin. (a) Pathologic slice at ×40 magnification. (b) Part of a ×200 field in a pathologic slice. Salient features of this fibroadenoma stage are few stromal cells (c in b), hyalinized collagen fibers (h in b), and compressed ducts (d in a).
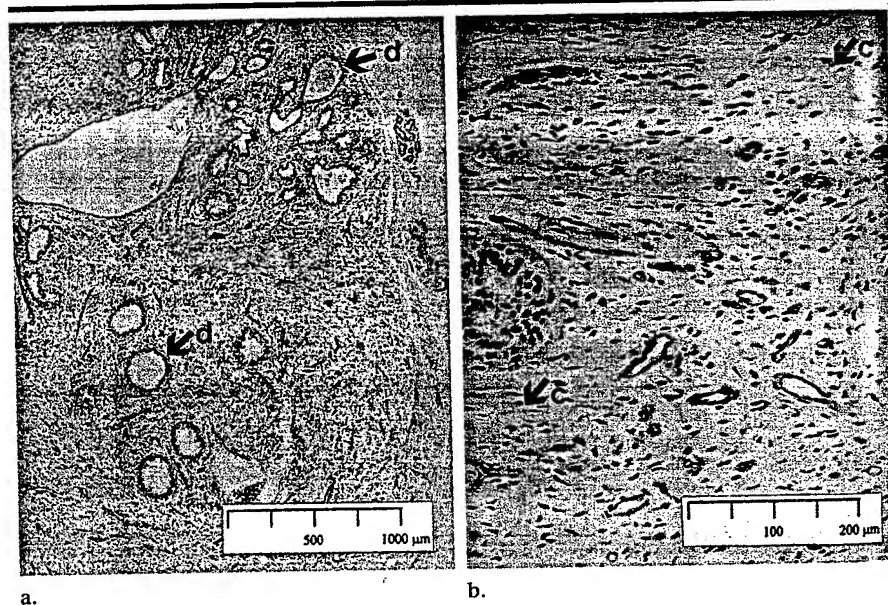

a.   b.

Figure 5. Case 22. Pathologic slices show a typical cellular fibroadenoma stained for factor VIII–related antigen and counterstained with hematoxylin. (a) Pathologic slice at ×40 magnification. (b) Part of a ×200 field in a pathologic slice. Salient features of this fibroadenoma stage are high numbers of stromal cells (c in b) and open ducts (d in a).

applicability of MR to predicting disease outcome rather than to determining whether a lesion is malignant or benign. We have evaluated microvessel density over entire tumors to provide more pertinent information for using these noninvasive techniques for diagnostic applications. While most recent work in which US has been used to image breast carcinoma has focused on color Doppler US, substantial improvements in vessel detectability are expected with the use of intravenous US contrast material, and it is possible that sensitivity will be increased

Figure 6. Case 7. Pathologic slice of an invasive carcinoma at ×40 magnification (stained for factor VIII–related antigen and counterstained with hematoxylin). Note the abundance of larger vessels (>200 μm; arrows) around the periphery.

to a level at which capillaries and other small microvessels will be visualized. Further gains in spatial resolution and vessel detectability with Doppler US and MR imaging will increase the potential for using these imaging modalities to identify tumor hot spots and noninvasively measure microvessel density.

While further histologic studies are necessary to evaluate vascular patterns in nonpalpable lesions, such as in atypical hyperplasia and carcinoma in situ, the results reported here suggest that the additional information on the spatial distribution of vessels and the ability to resolve vessel size may add valuable information to the diagnostic work-up of an indeterminate solid lesion. These examinations have important implications for younger women with palpable lesions, since diagnosis by using mammography is particularly unreliable in this age group and fibroadenomas are common.

References
1. Schmitt EL, Threatt B. Characteristics of breast cancer in an incident cancer population. AJR 1984; 143:402–406.
2. Xenophon L. Imaging techniques for breast disease. Clin Obstet Gynecol 1994; 37:933–943.
3. Baker LH. Breast cancer detection demonstration project: five-year summary report. CA Cancer J Clin 1982; 32:194–225.
4. Verbeek AL, Hendriks JH, Holland R, Mravunac M, Sturmans F, Day NE. Reduction of breast cancer mortality through mass screening with modern mammography: first results of the Nijmegen project, 1975-1981. Lancet 1984; 1:1222–1224.
5. Bassett LW, Kimme-Smith C. Breast sonography. AJR 1991; 156:449–453.
6. Jackson VP. The role of ultrasound in breast imaging. Radiology 1990; 177:305–309.
7. Jackman RJ, Nowels KW, Shepard MJ, Finkelstein SI, Marzoni FA. Stereotaxic large-core needle biopsy of 450 nonpalpable breast lesions with surgical correlation in lesions with cancer or atypical hyperplasia. Radiology 1994; 193:91–95.
8. Kopans DB. Caution on core. Radiology 1994; 193:325–328.
9. Williams SM, Kaplan PA, Petersen JC, Lieberman RP. Mammography in women under age 30: is there clinical benefit? Radiology 1986; 161:49–51.
10. Ciatto S, Cataliotti L, Distante V. Nonpalpable lesions detected with mammography: review of 512 consecutive cases. Radiology 1987; 165:99–102.
11. Furnival CM, Irwin JR, Gray GM. Breast disease in young women: when is biopsy indicated? Med J Aust 1983; 2:167–169.
12. Cant PJ, Madden MV, Coleman MG, Dent DM. Non-operative management of breast masses diagnosed as fibroadenoma. Br J Surg 1995; 82:792–794.
13. Heywang SH, Wolf A, Pruss E, Hilbertz T, Eiermann W, Permanetter W. MRI of the breast with Gd-DTPA: use and limitations. Radiology 1989; 171:95–103.
14. Burns PN, Halliwell M, Wells PN, Webb AJ. Ultrasonic Doppler studies of the breast. Ultrasound Med Biol 1982; 8:127–143.
15. Cosgrove DO, Bamber JC, Davey JB, McKinna JA, Sinnett HD. Color Doppler signals from breast tumors: work in progress. Radiology 1990; 176:175–180.
16. Dixon JM, Walsh J, Paterson D, Chetty U. Colour Doppler ultrasonography studies of benign and malignant breast lesions. Br J Surg 1992; 79:259–260.
17. Kaiser WA, Zeitler E. MRI of the breast: fast imaging sequences with and without Gd-DTPA—preliminary observations. Radiology 1989; 170:681–686.
18. Kubek KA, Chan L, Frazier TG. Color Doppler flow as an indicator of nodal metastasis in solid breast masses. J Ultrasound Med 1996; 15:835–841.
19. Holcombe C, Pugh N, Lyons K, Douglas-Jones A, Mansel RE, Horgan K. Blood flow in breast cancer and fibroadenoma estimated by colour Doppler ultrasonography. Br J Surg 1995; 82:787–788.
20. Flickinger FW, Allison JD, Sherry RM, Wright JC. Differentiation of benign from malignant breast masses by time-intensity evaluation of contrast enhanced MRI. Magn Reson Imaging 1993; 11:617–620.
21. Fearon ER, Vogelstein B. A genetic model for colorectal tumorigenesis. Cell 1990; 61:759–767.
22. Sato T, Akiyama F, Sakamoto G, Kasumi F, Nakamura Y. Accumulation of genetic alterations and progression of primary breast cancer. Cancer Res 1991; 51:5794–5799.
23. Dent DM, Cant PJ. Fibroadenoma. World J Surg 1989; 13:706–710.
24. Orel SG, Schnall MD, LiVolsi VA, Troupin RH. Suspicious breast lesions: MRI with radiologic-pathologic correlation. Radiology 1994; 190:485–493.
25. Buadu LD, Murakami J, Murayama S, et al. Breast lesions: correlation of contrast medium enhancement patterns on MR images with histopathologic findings and tumor angiogenesis. Radiology 1996; 200:639–649.
26. Frouge C, Guinebretiere JM, Contesso G, Di Paola R, Blery M. Correlation between contrast enhancement in dynamic magnetic resonance imaging of the breast and tumor angiogenesis. Invest Radiol 1994; 29:1043–1049.
27. Hulka CA, Smith BL, Sgroi DC, et al. Benign and malignant breast lesions: differentiation with echo-planar MR imaging. Radiology 1995; 197:33–38.
28. Weidner N, Semple JP, Welch WR, Folkman J. Tumor angiogenesis and metastasis: correlation in invasive breast carcinoma. N Engl J Med 1991; 324:1–7.
29. Ohtani H, Sasano N. Stromal cells of the fibroadenoma of the human breast. Virchows Arch 1984; 404:7–16.
30. Le Doussal V, Tubiana-Hulin M, Friedman S, Hacene K, Spyratos F, Brunet M. Prognostic value of histologic grade nuclear components of Scarff-Bloom-Richardson (SBR): an improved score modification based on a multivariate analysis of 1262 invasive ductal breast carcinomas. Cancer 1989; 64:1914–1921.
31. Less JR, Skalak TC, Sevick EM, Jain RK. Microvascular architecture in a mammary carcinoma: branching patterns and vessel dimensions. Cancer Res 1991; 51:263–273.
32. Jensen HM, Chen I, DeVault MR, Lewis AE. Angiogenesis induced by "normal" human breast tissue: a probable marker for precancer. Science 1982; 218:293–295.
33. Bosari S, Lee AKC, DeLellis RA, Wiley BD, Heatley GJ, Silverman ML. Microvessel quantitation and prognosis in invasive breast carcinoma. Hum Pathol 1992; 3:755–761.
34. Toi M, Kashitani J, Tominaga T. Tumour angiogenesis is an independent prognostic indicator in primary breast carcinoma. Int J Cancer 1993; 55:371–374.
35. Warren BA. The vascular morphology of tumors. In: Peterson HI, ed. Tumor blood circulation: angiogenesis, vascular morphology and blood flow of experimental and human tumors. Boca Raton, Fla: CRC, 1979; 1–48.
36. Ziche M, Gullino PM. Angiogenesis and neoplastic progression in vitro. J Natl Cancer Inst 1982; 69:483–487.
37. Brinck U, Fischer U, Korabiowska M, Jutrowski M, Schauer A, Grabbe E. The variability of fibroadenoma in contrast-enhanced dynamic MR mammography. AJR 1997; 168:1331–1334.
38. Nunes LW, Schnall MD, Orel SG, et al. Breast MR imaging: interpretation model. Radiology 1997; 202:833–841.
39. Heywang-Kobrunner SH, Haustein J, Pohl C, et al. Contrast-enhanced MR imaging of the breast: comparison of two different doses of gadopentetate dimeglumine. Radiology 1994; 191:639–646.
40. Gasparini G, Harris AL. Clinical importance of the determination of tumor angiogenesis in breast carcinoma: much more than a new prognostic tool. J Clin Oncol 1995; 13:765–782.

Appendix 2

Quantitative Diffusion Imaging in Implanted Human Breast Tumors

Cynthia F. Maier, Yael Paran, Peter Bendel, Brian K. Rutt, Hadassa Degani

Quantitative diffusion measurements were performed in tumors arising from inoculation of nude mice with two human breast cancer cell lines (MCF7 and T47D) to evaluate the specificity of this technique for characterizing solid tumors. ADC maps were compared to histology and correlated well with gross tumor morphology. Measured ADCs were highly specific for viable and necrotic tumor in the five T47D tumors included in this study ($P < 0.02$), while only two of the five MCF7 tumors studied developed distinguishable areas of necrosis. No statistically significant difference was observed in ADCs from viable tumor between the different cell lines ($P > 0.05$).

Key words: magnetic resonance imaging; diffusion; breast cancer; necrosis.

INTRODUCTION

Magnetic resonance diffusion imaging is a technique that has recently been applied to imaging human tissues *in vivo*. The rate of water diffusion in tissue directly reflects intrinsic tissue parameters such as tissue microstructure and the degree of water compartmentalization, and the concentration of proteins and macromolecules in the water's environment. In tumors, water diffusion is an important process that has implications for nutrient delivery and clearance.

Preliminary diffusion measurements in animal tumor models using MRI have demonstrated potential for providing information about gross tumor morphology and for detecting tumor necrosis (1–3). It has been suggested that tumor response to chemotherapy or radiation therapy could be monitored non-invasively using an MR-imaging technique based on diffusion (3). To date, however, most spatially resolved, *in vivo* studies of water diffusion have been based on a single diffusion-weighted image, which provides only qualitative information. A more quantitative approach is necessary, where apparent diffusion coefficients (ADCs) are measured with high

spatial resolution for the tumor and the specificity of these ADCs for characterizing tumors is assessed. In recent work by Eis *et al.* (4), quantitative analysis of the ADC in rat brain tumors demonstrated potential for differentiating tumors from normal brain tissue. However, the low spatial resolution of images in this study did not allow differentiation of morphologically distinct features (e.g., areas of necrosis or fibrosis) within the tumors.

The purpose of this work was to demonstrate the potential for diffusion imaging as a method for characterizing solid tumors, and for providing information about tumor morphology on a cellular level. We evaluated water diffusion by using MRI in two different mouse tumor models of human breast cancer (MCF7 and T47D cell lines). A range of tumor sizes were studied, where some of the tumors were allowed to grow to large sizes, resulting in cell death and necrosis in the interior of the tumor. ADC maps were calculated for the tumors, and average ADCs measured for regions of viable neoplastic tissue and for necrosis. These quantitative diffusion measurements were compared to histopathology and the specificity of the ADC for identifying different tumor components was evaluated.

MATERIALS AND METHODS

Tumor Model

MCF7 and T47D human breast cancer cells were cultured and prepared for inoculation as described previously (5, 6). Ten female CD1-NU athymic mice (8 weeks old), were subcutaneously inoculated in the mammary fat pad with approximately 10^7 cells in a volume of 0.4 ml (five mice for each tumor model). Before injection of the cancer cells, a pellet of 17β estradiol was implanted under the skin of the back (0.72 mg/pellet, 60 day release, Innovative Research of America, Sarasota, FL) to facilitate tumor growth. The tumors were allowed to develop for 4–12 weeks, to sizes ranging between 0.5 and 2.0 cm in diameter. In larger tumors, regions of necrosis developed mainly in the centers of the tumors, presumably as a result of inadequate nutrient and oxygen delivery to these areas.

MRI Measurements

Mice were anesthetized before imaging by using Pental diluted in PBS solution (Pentobarbitone sodium, CTS Chemical Industries, Tel-Aviv, Israel) by an intraperitoneal (IP) injection (0.06 mg/g). Follow-up injections (0.03 mg/g) were administered IP on an hourly basis after the initial injection, via an infusion line that extended outside the imager. To prevent motion during the examination, the mice were immobilized for the course of the MR experiments by laying them in prone position on a home-

made mouse tray and taping the lower half of the body securely to the tray. The upper abdomen and chest were not constrained so that respiration would not be impaired. A water standard was placed near the tumor for each of the experiments. The room temperature was maintained during the examination at 25–30°C.

¹H MR images of the tumors were collected at 4.7 Tesla by using a horizontal bore Biospec 4.7/30 animal imager (Bruker, Karlsruhe, Germany), and a custom-built 7.5-cm diameter radiofrequency (RF) coil. Gradient hardware consisted of unshielded gradient coils with a maximum gradient strength of 48 mT/m at a rise time of 500 μs, using standard gradient pre-emphasis provided by the manufacturer. A transverse pilot scan was used to define coronal slices covering the whole tumor. A standard multislice PGSE sequence was used with $TE/TR = 48$ ms/2400 ms, $\Delta = 22.4$ ms, $\delta = 16.2$ ms (Δ and δ are defined as in Fig. 1). TE was kept as short as possible to minimize signal loss due to T_2 relaxation (our previous measurements of T_2 in these tumors gave an average value of approximately 68 ms). A series of 13 diffusion-weighted images was obtained, with diffusion b values ranging from $b = 0$ s/mm^2 to $b = 754$ s/mm^2 ($b = \gamma^2 g^2 \delta^2 (\Delta - \delta/3)$, where γ is the magnetogyric ratio and g is the diffusion-encoding gradient strength as defined in Fig. 1). Nine of these 13 images were sensitized to incoherent blood flow with b values less than 220 s/mm^2 (7–10). Diffusion-weighting was varied by changing the amplitude of the diffusion gradients while keeping all timing parameters constant. Phase-cycling was performed to cancel the effects of RF inhomogeneities on the 180° refocusing pulse. Images were obtained with 3 cm field of view, slice thickness of 1 mm, a matrix size of 64 × 256 pixels (in-plane resolution of 472 × 118 μm) and two averages for an acquisition time of 5 min. and 10 s. The raw data were zero-filled and Fourier transformed to give images with 256 × 256 pixels.

For the imaging gradient strengths required at this spatial resolution, significant systematic errors are introduced into the determination of diffusion coefficients by the interaction of the imaging gradients with the diffusion gradients (11, 12). We employed a method for eliminating this contribution to the b weighting that was first proposed by Neeman *et al.* (13), where images are acquired by using both positive and negative diffusion gradients for each b value and the geometric average of these images is calculated. This method also allows the elimination of unwanted contributions to the b value from the interaction of the diffusion gradients with background gradients arising from susceptibility variations within the sample.

Following the diffusion imaging sequence, high-resolution T_2-weighted spin echo images were acquired for the same slice locations to provide a reference for the diffusion data. Such T_2-weighted images have previously been correlated with histology (5) and allow identification of necrotic regions, viable tumor, and fibrous tissue. The images were acquired using $TE/TR = 68$ ms/2400 ms, matrix size = 128 × 256 pixels (in-plane resolution of 236 × 118 μm) and four averages. The other parameters were as for the diffusion images. The acquisition time for the T_2-weighted images was 20 min. The total

length of time required for the MR examination including setup and localizers was approximately 3 h per animal.

Image Analysis

Images were transferred to a DEC 3000 workstation for analysis where image analysis was performed by using MATLAB software Version 4.2 (The Mathworks, Inc. Natick, MA). One image for each b value was obtained by geometrically averaging positive-gradient and negative-gradient images according to the method proposed by Neeman (13).

Average ADCs were calculated for regions of interest (ROIs) in areas that were identified as viable or as necrotic by comparison to the high-resolution T_2-weighted scans. These regions were selected on the T_2-weighted scan based on their relative signal intensities, and morphological appearance. The regions were selected as being "clearly" identifiable as either necrotic or viable. Where possible, one ROI for each of viable and necrotic tissue were chosen per slice. For these calculations, the standard deviation of signal intensities within the ROI was taken as the uncertainty in the mean signal intensity. Fits having $r < 0.97$ (14) were rejected. The ADC of the water standard was obtained as a reference for each tumor.

Maps of the apparent diffusion coefficient were calculated for each slice on a pixel-by-pixel basis from the slope of a linear least-mean-squares fit of the natural logarithm of signal intensity to the b factor. The noise in signal intensity for each pixel was estimated by the standard deviation of signal intensities in a ROI in the background.

Histology

Immediately after the MR imaging experiments, two mice with MCF7 tumors and two mice with T47D tumors were sacrificed to provide a comparison to histology. The tumors were surgically removed, fixed in 10% formaldehyde solution, imbedded in paraffin, and sectioned to correspond to the MR imaging planes. Representative
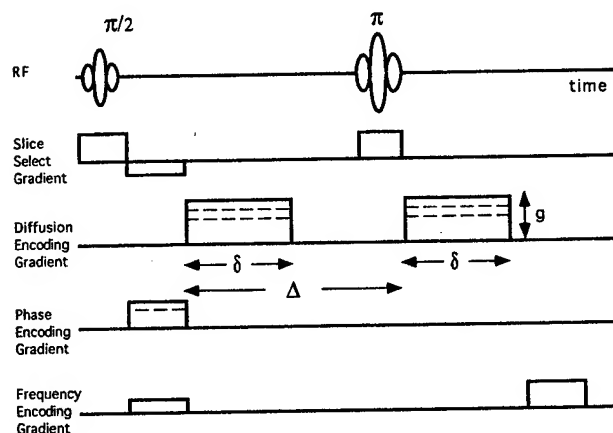

FIG. 1. Multislice PGSE sequence used for diffusion measurements. *TE/TR* for the sequence = 48 ms/2400 ms, $\Delta = 22.4$ ms, $\delta = 16.2$ ms. Diffusion-encoding gradients were on the slice-select axis.
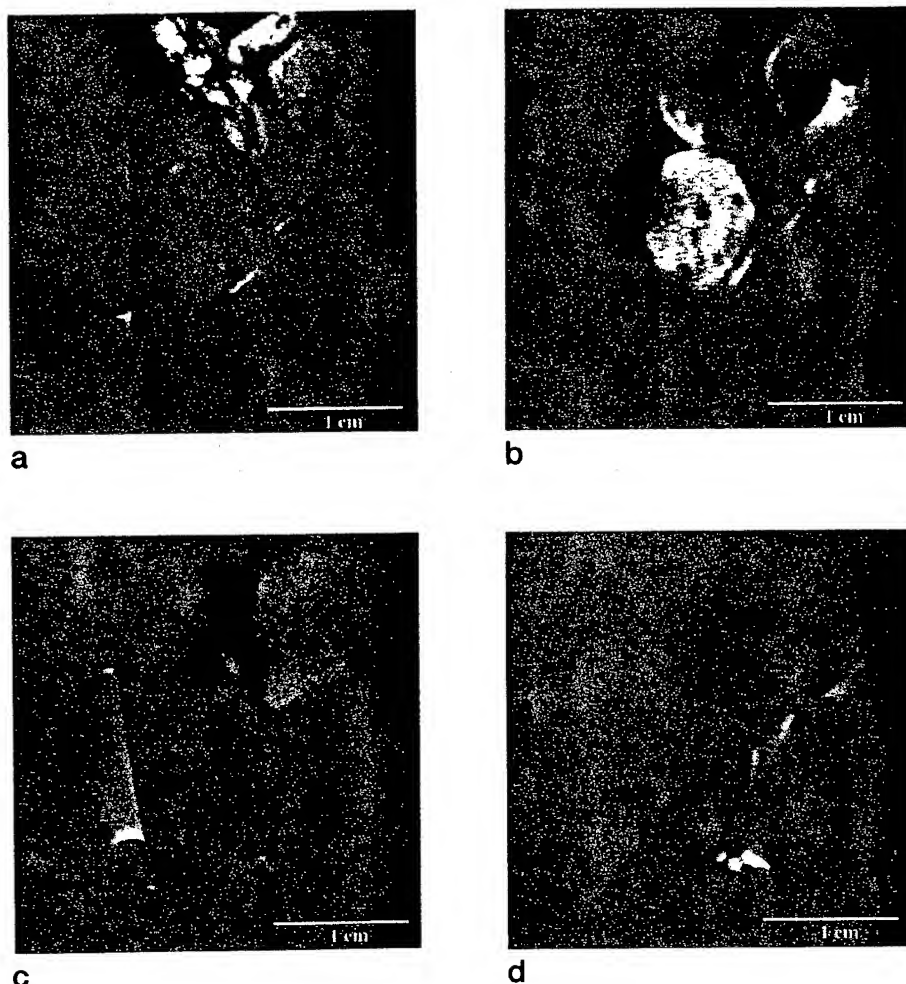
FIG. 2. Representative MR images from implanted breast tumors. (a) T_2-weighted image of a 4-week-old MCF7 tumor (M3) with 128 phase encodes. (b) Diffusion-weighted image of tumor M3 with $b = 636$ s/mm² and 64 phase encodes. (c) A T_2-weighted image of a 4-week-old T47D tumor (T5) with 128 phase encodes. (d) Diffusion-weighted image of tumor T5 with $b = 636$ s/mm² and 64 phase encodes.

crosis was present in the T47D tumors than in MCF7 tumors having similar age and size.

Typical image signal-to-noise for viable tumor ranged from 60:1 on $b = 0$ s/mm² images to 40:1 on $b = 754$ s/mm² images (where the noise was estimated from the standard deviation in a ROI in the background). Areas of necrosis could be identified as having increased signal intensity on the T_2-weighted images (15, 16), and reduced signal intensity on the higher diffusion-weighted images. MCF7 and T47D tumors had similar appearances for all imaging sequences. Representative images are shown in Fig. 2. Figures 2a and 2b show a 4-week-old MCF7 tumor (M3), where Fig. 2a is a high-resolution T_2-weighted image, and Fig. 2b is a lower resolution diffusion-weighted image ($b = 636$ s/mm²). Figures 2c and 2d show a 4-week-old T47D tumor (T5) for comparison.

Motion artifacts due to breathing were visible in the upper abdominal region, but very little phase-smearing was observed in the region of the tumor. Motion of the tumor occurring between scans was limited to a few pixels over the entire set of b values. This motion was qualitatively evaluated by outlining the tumor on the $b = 0$ image, and displaying this outline on subsequent images.

Mean ADCs were calculated for viable and necrotic regions within the tumors to determine the specificity of the ADC for characterizing the tissue. Figure 3a shows typical ROIs defined on a high-resolution T_2-weighted image in water, viable tumor, and necrotic tumor for a 3-week-old T47D tumor (T_2). A histological section stained with H&E corresponding to this image is shown in Fig. 3b. The beginning of necrotic regions near the center of the tumor is evident even though this tumor is relatively young. A semilog plot of the mean signal intensities within these ROIs is shown in Fig. 3c. 200 × magnification views of hematoxylin-eosin-stained histological sections corresponding to these regions are shown in Figs. 3d and 3e. Figure 3d shows a region of viable tumor and Fig. 3e corresponds to the necrotic center of the tumor.

4-μm thick slices from each section were stained with Hematoxylin-Eosin and by using a modified trichrome technique to stain mucopolysaccharides of fibrous tissue.

RESULTS

In previous work in our laboratory (5, 15–17), we studied a tumor model where breast cancer cells were implanted in the mouse flank. Tumors from both cell lines that were studied in this work developed faster in the mammary fat pad than had previously been observed in the flank. Average ages and diameters for the 10 tumors included in this study are given in Table 1. After 4 weeks, most of the tumors had reached a size of 0.5–1.0 cm in diameter. In 6- to 8-week-old tumors, it was possible to see regions of necrosis, usually near the center of the tumor. These could be observed both on the T_2-weighted images, and on the highly diffusion-weighted images. After 11 weeks, one of the MCF7 tumors had reached a size of 2.5 cm in diameter, and developed a large necrotic core. More ne-

ROIs were defined in viable and necrotic tissue on as many slices as possible (as selected on the T_2-weighted images) and mean ADCs for these regions are shown in
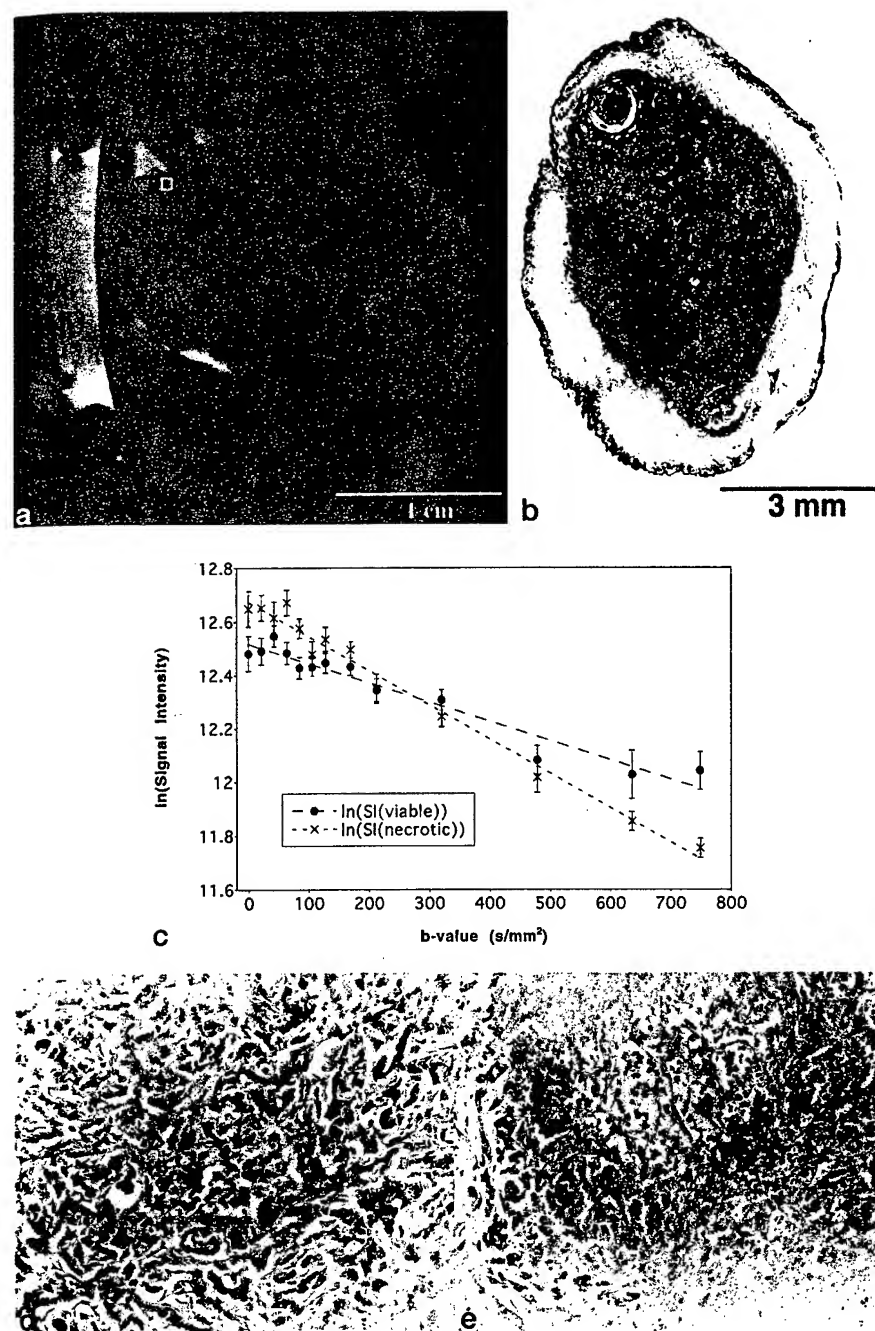
FIG. 3. (a) T_2-weighted image of a 3-week-old T47D tumor (T2). Typical ROIs are shown outlining regions containing water, viable tumor (white), and necrosis (black). (b) Low-magnification view of a H&E-stained histological section corresponding to this image. Areas of necrosis are marked with arrows. (c) Mean signal intensities within these ROIs for $b = 0$ to 754 s/mm^2. (d)-(e) 200 × magnification views of the H&E-stained sections corresponding to viable tumor and necrosis, respectively.

between ADCs of necrosis and viable tissue for all T47D tumors ($P < 0.02$ using a Mann-Whitney Rank Sum Test). Since easily identifiable necrotic regions were present only on two MCF7 tumors, no statistical test was performed to compare between necrotic and viable tumor for MCF7. There was no statistically significant difference in calculated ADCs of viable tumor between MCF7 tumors and T47D tumors ($P > 0.05$ using a standard t test).

ADC maps were calculated from a straight-line fit of the natural logarithm of the signal intensity to the diffusion-weighting b factor on a pixel-by-pixel basis. These maps show significant contrast between areas of necrosis and areas of viable tumor, and provide a highly detailed representation of gross tumor morphology. Representative ADC maps are shown in Fig. 4. Figures 4a and 4b show one slice from an 8-week-old MCF7 tumor (M4), which has begun to develop small regions of necrosis near its center. Figure 4a is an ADC map, while Fig. 4b shows a histogram with the distribution of ADCs within the tumor. The results from an older, 11-week-old MCF7 tumor (M5) with a large necrotic center are shown in Figs. 4c and 4d. Two distinct peaks corresponding to the viable and necrotic areas are visible in the histogram for this tumor. These ADC maps show good correlation with gross morphological features of the tumors, as observed on the histological slices. No consistent biexponential signal decay could be observed within the tumor, even in regions showing high vascularity on histology where the contribution to the signal from blood flowing in the microcirculation would be expected to be strongest. In many pixels, a signal increase was observed at low b values, likely indicating that small macroscopic motions had occurred between scans.

DISCUSSION

Tumors from both cell lines grew faster and larger in the mammary fat pad than had previously been observed in

Table 1. The standard error in the mean for these measurements is reported as the experimental uncertainty. Water ADCs were calculated as a reference for each tumor, and reflect the range of temperatures within the bore for the experiments. The signal decay from the water standards was highly linear. No attempt was made to correct measured ADCs in tumors for temperature, since the tumor is assumed to be affected little by the ambient temperature. The results show a well-defined separation

Table 1

Measured Apparent Diffusion Coefficients for Regions of Interest in T47D and MCF7 Human Breast Tumors

| Tumor	Diameter (cm)	Apparent Diffusion Coefficients		
		Water (10^{-3} mm²/s)	Necrosis (10^{-3} mm²/s)	Viable tumor (10^{-3} mm²/s)
T47D				
T1 (3 weeks)[a]	1.0	2.10 ± 0.07[b]	2.00 ± 0.07	0.68 ± 0.03
T2 (3 weeks)	1.0	2.55 ± 0.02	1.46 ± 0.06	0.69 ± 0.06
T3 (4 weeks)	0.4	2.52 ± 0.04	1.57 ± 0.08	0.49 ± 0.01
T4 (4 weeks)	0.5	2.35 ± 0.02		0.51 ± 0.07
T5 (5 weeks)	1.0	2.36 ± 0.03	1.49 ± 0.12	0.49 ± 0.04
Mean value			1.63 ± 0.12	0.57 ± 0.05
MCF7				
M1 (4 weeks)	0.7	2.34 ± 0.18		0.47 ± 0.02
M2 (4 weeks)	0.8	2.49 ± 0.07	1.26 ± 0.08	0.44 ± 0.05
M3 (4 weeks)	1.0	2.32 ± 0.10		0.48 ± 0.04
M4 (8 weeks)	1.5	2.36 ± 0.08		0.49 ± 0.02
M5 (11 weeks)	2.5	2.25 ± 0.05	1.30 ± 0.12	0.43 ± 0.04
Mean value			1.28 ± 0.02	0.46 ± 0.01

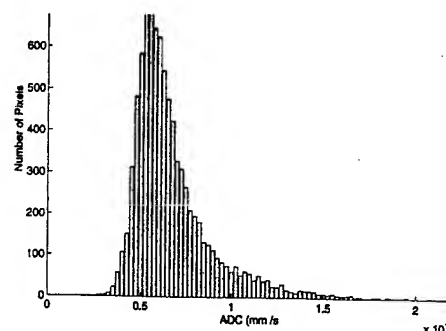[a] The tumor age refers to the time from day of implantation to the day of measurement.
[b] The standard deviation of pixel intensities within the ROI is reported as the measured uncertainty. For all ROIs, n > 25 pixels.
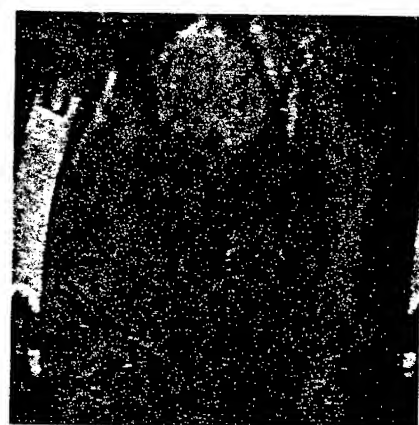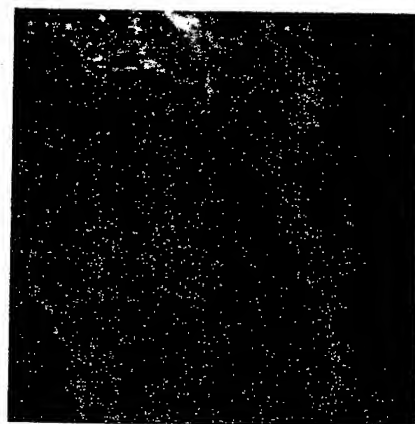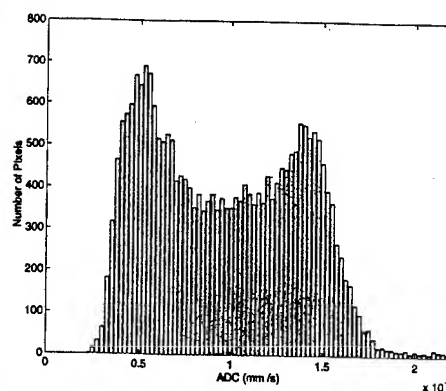

FIG. 4. (a) ADC map of an 8-week-old MCF7 tumor (M4), which has begun to develop small regions of necrosis near its center (areas of high signal intensity). (b) Histogram showing the distribution of ADCs within the tumor. (c)-(d) The results from an older, 11-week-old MCF7 tumor (M5) with a large necrotic center. (c) ADC map, (d) ADC histogram.

the flank. MCF7 tumors grew faster and to a larger size than corresponding T47D tumors in this study. We hypothesize that this is due to better nutrient and oxygen delivery, as a result of increased vascularity in MCF7 tumors. More blood vessels were apparent on histology in MCF7 tumors than T47D. In general, more necrosis was present in T47D tumors, and even highly necrotic regions in the MCF7 tumors contained more cellular debris, and islands of viable tumor cells, indicating more recently formed necrosis.

Measured ADCs were highly specific for necrotic and viable tumor in both MCF7 and T47D tumors. The higher diffusion rates in necrotic areas reflect increased volume of extracellular space and increased mobility of water molecules in the extracellular compartment. The tortuosity of the extracellular compartment is reduced in necrosis compared with viable neoplastic tissue due to the decreased density of cells. Additionally, the relative volume fraction of water in the extracellular space is greatly increased in necrotic regions due to cell lysis. In addition to being specific for identification of necrotic regions, it is plausible that the measured ADC is an indication of the stage of the necrosis. In initial stages of the formation of necrosis, the cells and cytoplasmic compartments swell and the nucleus may shrink and become fragmented. After disruption of the cell membrane, the cell contents are released and cellular details are lost. This results in the appearance of sparsely distributed nuclear dust, membrane fragments and proteins. In addition, in most cases we could observe islands of still viable cells within the necrotic regions. However, the spatial variation of these morphologically distinct features occurs on a scale much smaller than the slice

thickness of 1 mm. Therefore, the measured ADC for a pixel may reflect water mobility at all stages of necrosis, as well as in viable tumor.

Although no statistically significant difference was observed between viable tumor in MCF7 and T47D tumors, the measured ADCs in necrotic regions in T47D tumors were higher than in corresponding necrotic regions in MCF7 tumors. This is consistent with what is expected from partial volume effects since the necrosis found in T47D tumors was, in general, more progressed than that found in MCF7 tumors and is therefore expected to be more edematous.

ADC maps showed relatively uniform signal intensities within areas of necrotic and viable tumor, and excellent contrast was observed between necrotic regions within the tumors and areas of viable neoplastic tissue. The maps compared well to gross tumor morphology as evidenced by histological sections corresponding to the images. A more detailed comparison to histology could not be made because of the difference of a factor of 200 in slice thickness between the MR images and histological slices. The existence of small macroscopic motions of the tumor occuring between scans during the long examination times precluded an investigation of IVIM effects for this data.

The results suggest that diffusion-weighting imaging, with an appropriate choice of weighting parameters could provide a valuable noninvasive technique for characterizing tumor response to therapy. Currently, locally advanced cancer is managed by using a combined modality treatment including multiagent chemotherapy, surgery, and radiation. Unfortunately, the response of the tumors to these therapies is highly variable, and not well-predicted, making individual treatment planning a very difficult problem. Tumor response to therapy is evaluated conventionally by a combination of clinical examination and x-ray techniques. However, tumor response in the form of cell death and necrosis precedes changes that can be detected by using these methods, and in many cases, a large degree of necrosis can occur with no detectable change in size or radiographic appearance. With the development of specialized gradient coil hardware to provide adequate diffusion weighting (18), it is likely that diffusion imaging by using MR can be used in a clinical setting to more efficiently monitor tumor response to therapy.

CONCLUSIONS

We have applied MR diffusion imaging techniques to human breast cancer implanted in nude mice. The results of this study indicate that the ADC as measured by using a PGSE sequence is specific for necrosis and viable tumor. Maps of the ADC reflected well the gross morphological features of the tumors as revealed by histological examination. The results indicate potential for characterizing solid tumors by using diffusion imaging, and may have implications for monitoring tumor response to therapy.

REFERENCES

1. K. G. Helmer, B. J. Dardzinski, C. H. Sotak, Time dependent diffusion in RIF-1 tumors: in vivo extraction of geometrical parameters and identification of necrosis, in "Proc., SMR, 2nd Annual Meeting, San Francisco, 1994," p. 1044.

2. J. Dunn, S. Ding, J. O'Hara, K. Liu, E. Rhodes, J. Weaver, H. Swartz, The apparent diffusion coefficient measured by MRI correlates with pO_2 in a RIF-1 tumor. *Magn. Reson. Med.* **34**, 515–519 (1995).

3. M. Zhao, J. G. Pipe, J. Bonnett, J. L. Evelhoch, Early detection of treatment response by diffusion-weighted ^{1}H-NMR spectroscopy in a murine tumor in vivo. *Br. J. Cancer* **73**, 61–64 (1996).

4. M. Eis, T. Els, M. Hoehn-Berlage, High resolution quantitative relaxation and diffusion MRI of three different experimental brain tumors in rat. *Magn. Reson. Med.* **34**, 835–844 (1995).

5. E. Furman, R. Margalit, P. Bendel, A. Horowitz, H. Degani, In vivo studies by magnetic resonance imaging and spectroscopy of the response to tamoxifen of MCF7 human breast cancer implanted in nude mice. *Cancer Commun.* **3**, 287–297 (1991).

6. H. Degani, S. M. Ronen, E. Furman-Haran, Breast cancer: spectroscopy and imaging of cells and tumors, in "NMR in Physiology and Biomedicine" (R. J. Gillies, Ed.), pp. 329–352, Academic Press, San Diego, 1994.

7. D. LeBihan, E. Breton, D. Lallemand, P. Grenier, E. A. Cabanis, M. Laval-Jeantet, MR imaging of intravoxel incoherent motions: application to diffusion and perfusion in neurologic disorders. *Radiology* **161**, 401–407 (1986).

8. J. J. Neil, J. H. Ackerman, Detection of pseudodiffusion in rat brain following blood substitution with perflurocarbon. *J. Magn. Reson.* **97**, 194–199 (1992).

9. D. R. Pickens, D. Jolgren, C. H. Lorenz, J. L. Creasy, R. R. Price, MR perfusion imaging of an excised animal kidney. *Invest. Radiol.* **27**, 287–292 (1992).

10. D. Le Bihan, Intravoxel incoherent motion imaging. in "Diffusion and Perfusion Magnetic Resonance Imaging: Applications to Functional MRI" (D. Le Bihan, Ed.), pp. 270–274, Raven Press, New York, 1995.

11. M. Neeman, J. P. Freyer, L. O. Sillerud, Pulsed-gradient spin-echo diffusion studies in NMR imaging: effects of the imaging gradients on the determination of diffusion coefficients. *J. Magn. Reson.* **90**, 303–312 (1990).

12. M. Eis, M. Hoehn-Berlage, Correction of gradient crosstalk and optimization of measurement parameters in diffusion MR imaging. *J. Magn. Reson.* **107**, 222–234 (1995).

13. M. Neeman, J. P. Freyer, L. O. Sillerud, A simple method for obtaining cross-term-free images for diffusion anisotropy studies in NMR microimaging. *Magn. Reson. Med.* **21**, 138–143 (1991).

14. P. R. Bevington, D. K. Robinson, "Data Reduction for the Physical Sciences," McGraw-Hill Book Company, New York, 1992.

15. H. Degani, E. Furman, S. Fields, Magnetic resonance imaging and spectroscopy of MCF7 human breast cancer: pathophysiology and monitoring of treatment. *Clin. Chim. Acta* **228**, 19–33 (1994).

16. E. Furman-Haran, A. F. Maritzek, I. Goldberg, A. Horowitz, H. Degani, Tamoxifen enhances cell death in implanted MCF7 breast cancer by inhibiting endothelium growth. *Cancer Res.* **54**, 5511–5514 (1994).

17. E. Furman-Haran, R. Margalit, A. F. Maretzek, H. Degani, Angiogenic response of MCF7 human breast cancer to hormonal treatment: assessment by dynamic Gd-DTPA-enhanced MRI at high spatial resolution. *J. Magn. Reson. Imaging* **6**, 195–202 (1996).

18. C.F. Maier, H.N. Nikolov, B.K. Rutt, Practical design of a high-strength gradient coil for diffusion/microvascular imaging of breast tumors, in "Proc., SMR and ESMRMB, 3rd Annual Meeting, Nice, 1995," p. 312.

Appendix 3

Practical Design of a High-Strength Breast Gradient Coil

Cynthia F. Maier, Hristo N. Nikolov, Kenneth C. Chu, Blaine A. Chronik, Brian K. Rutt

A high-strength three-axis local gradient coil set was constructed for MRI of the breast. Gradient fields with good uniformity (<10% deviation from the desired gradient) over most of the volume required for breast imaging were generated with efficiencies of up to 3.3 mT/m/A. The coils will allow diffusion breast imaging in clinically acceptable examination times. The electrical design, water cooling system, and fabrication techniques are described. Preliminary tests of the coil included images of a grid phantom and diffusion measurements in a short-T_2 agarose gel phantom.

Key words: breast imaging; diffusion imaging; gradient coils.

INTRODUCTION

In this paper, we present a specialized gradient coil design for breast imaging and demonstrate the utility of this coil for performing MR diffusion imaging with short-duration, high-strength gradient pulses. Sensitization of an MR pulse sequence to motion can be achieved using conventionally available gradient hardware; however, measurement of water diffusion (or slow flow in microvessels) with this hardware requires long echo times to achieve large gradient moments and therefore suffers from significant signal loss due to T_2 relaxation and system nonidealities. In addition, increasing the time between motion-sensitizing gradient pulses allows more macroscopic motion to occur in this interval, resulting in pixel misregistration, motion-induced ghost artifacts, and diffusion/flow measurement artifacts. Higher-strength gradients will allow adequate sensitization to small motions (i.e., large gradient moments) with very short, high-amplitude gradient pulses and minimal time delay between these pulses.

METHODS

The gradient coil assembly was designed in a cylindrical geometry, with each gradient coil built onto a separate cylindrical former. The three-axis coil set was composed of concentrically nested coils, oriented vertically such that their common axis was transverse to the main field as shown in Fig. 1. Space restrictions within the magnet bore require that the coils be as short as possible in the vertical direction to allow a patient to lie comfortably above the top edge of the cylinders. Unfortunately, decreasing the height of the coils (relative to their diame-

ters) makes the creation of uniform gradients within the coils much more difficult. To satisfy the competing demands of good gradient uniformity and height restrictions, we used an aspect ratio of approximately 1:1 for our cylindrical coils. The height of the complete coil assembly was 16 cm, leaving 34-cm clearance in the vertical direction in our General Electric (GE) Signa Horizon scanner (General Electric Medical Systems, Milwaukee, WI), and the largest coil diameter was 21.6 cm.

To generate the winding densities required for high gradient strengths, relatively small-diameter wire (AWG no. 20) was used to construct the coils. The resistivity of this wire is high, requiring an active cooling system to remove heat and maintain temperatures inside the coils within a range comfortable for the patient. Water-cooling jackets with very thin walls were sandwiched between the gradient coils, so that resistive heat could be removed efficiently while maintaining the compact construction of the coil assembly. A dedicated RF coil and shield were mounted inside the innermost gradient coil with an approximately 1.3-cm space between the RF coil and closest gradient coil. The entire assembly is depicted in cross-section in Fig. 2.

Electrical Design

The highly efficient quadrupolar current distribution (1–3) was used to provide gradients in B_z along both the x and z directions (G_x and G_z). This current density varies azimuthally as $\cos(2\theta)$ and is entirely directed along the axial direction on the surface of the cylindrical former. Discrete wire positions approximating the continuous quadrupolar current density were calculated by sampling the current density $\cos(2\theta)$ at θ_i such that $\cos(2\theta_{i+1}) - \cos(2\theta_i)$ was constant. A schematic diagram showing this ideal wire distribution is given in Fig. 3a. The current pattern in Fig. 3a is nonphysical in that the current is discontinuous at the ends of the coil, and therefore, connecting paths between the wires ("return wires") must be provided. In most imaging applications in which local gradient coils have been used previously, the volume to be imaged has been located at the center of the coil, and placing return paths near the ends of the cylinder had a minimal effect on the desired field within the object. For breast imaging applications, the required location for the region of good gradient uniformity is near the top edge of the coils and a conventional return wire arrangement would corrupt the gradient field uniformity within this volume. We chose to place the return wire components instead on horizontal plates at the tops and bottoms of the coils. Close to the cylinders on the plates, the return paths were extended along the z direction for at least 5 cm (no B_z is generated by current in the z direction). The bottom set of return wires for the G_z coil were strung across the bottom of the cylinder in the z direction. The quadrupole current distribution for G_x is rotated 45° with respect to G_z, and the return wires for G_x could not be strung in the z direction; therefore, these wires were located on a horizontal plate.
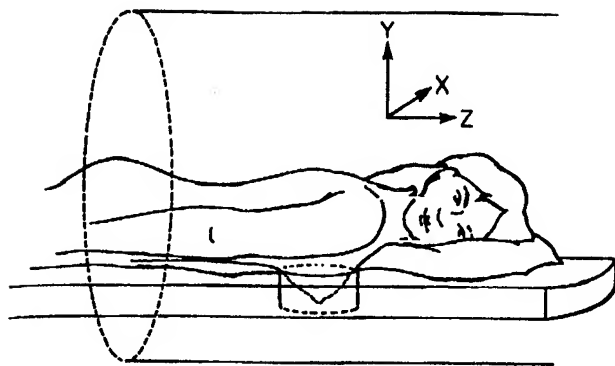
FIG. 1. Schematic showing orientation of local breast gradient coil in magnet.

The design of the G_y gradient makes use of the fact that $\nabla \times B = 0$ throughout any region in which the current density is 0. This means that a transverse gradient coil with its axis along z (the conventional orientation) can be turned 90° about the x axis so that its axis is along the y direction and used to produce a gradient in B_z along the y direction. We designed a transverse gradient coil in the conventional orientation using the target field method (4, 5) and then rotated the coil to produce G_y. Although a wide range of breast sizes exist, we defined an average volume of interest (VOI) for breast imaging (by comparison with commercially available breast RF coils) as a cylindrical volume with length equal to 60% of the coil height (11.5 cm), a diameter equal to 90% of the RF coil diameter (13.5 cm), and location flush with the top surface of the gradient coil assembly. The target field coil was designed to have its region of good gradient uniformity centered on this VOI. This design consisted of only two sets of closed current loops (Fig. 3b). For the target-field coil in its conventional orientation with its axis along z, the desired gradient is created almost entirely by the current in half of the wire loops only (the "primary" component of the loop as indicated in Fig. 3b), and return wires are an intrinsic part of the design (labeled "return" in Fig. 3b). For this coil, only one set of "return paths" is required for current continuity, and in the vertical orien-
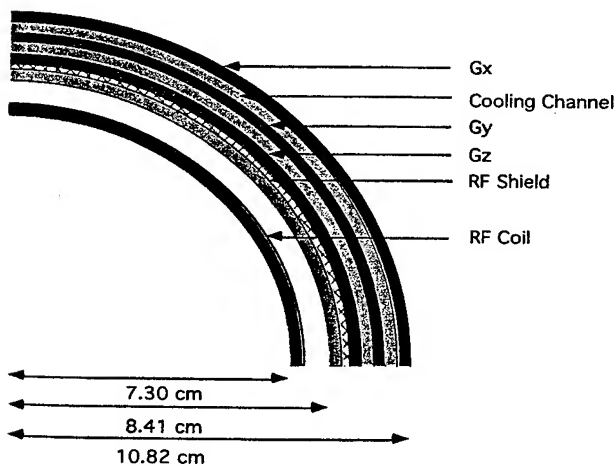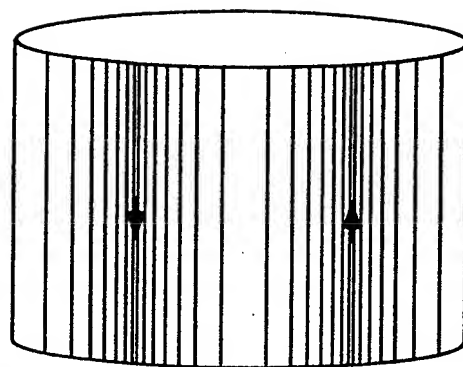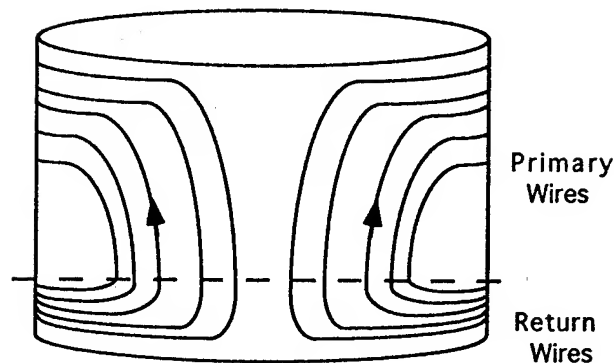

FIG. 2. Cross-section of complete gradient coil assembly showing location of RF coil and water-cooling modules.

FIG. 3. (a) Quadrupolar current density with 56 windings. (b) Target-field-design transverse coil. The "primary wire" component is almost entirely responsible for generation of the transverse gradient for the conventional coil orientation with its axis along z.

tation, these wires are located at the bottom of the cylinder. In our coil design, such a large number of loops was required to generate the desired gradient efficiency that these return wires would have occupied a large fraction of the space available on the surface of the cylinder. Due to the strict limitations on coil height, we believed that this space could be used more efficiently if only the primary component of the coil design was present on the cylinder itself and the return paths were located on a horizontal plate as for the quadrupole coils. A complication that arises from truncating the wire pattern in the vertical dimension in this way is that the reciprocity relations from Maxwell's equations no longer hold for a nonphysical current distribution (i.e., $\nabla \times B \neq 0$ for a current distribution with nonzero divergence). This means that the gradient field calculated for the truncated design is not identical in the conventional and transverse orientations unless the return wires are included in the calculation. We shall see in the Results section that the truncated coil in the transverse orientation has both an increased gradient efficiency compared to the full design for the same coil height and, additionally, the region of acceptable gradient uniformity (<20% deviation from uniformity) is significantly larger for the truncated coil.

One undesirable side effect that arises from locating the return wires on horizontal surfaces is that the torque on the coils from interaction with the main static field is greatly increased. This effect is significant. For our 1.5-T

magnet, current is only supplied when the coils are positioned near the central, highly homogeneous region of the magnet (typical clinical imaging systems have a 50-cm-diameter spherical volume of better than 10 ppm B_0 uniformity) and the upward (downward) force on the $+z$ ($-z$) half of the horizontal plate for the G_z coil is approximately 15 N/A (3.5 lb/A) increasing linearly with applied current. As the gradients are switched, the effect of this force is to create an alternating torque of approximately 3 Nm/A in size. For many pulse sequences, the direction of the current is switched rapidly, resulting in a torque that alternates direction rapidly and causes significant vibrational stress on the coils. For our preliminary experiments, a temporary coil support was constructed from wood- and glass-reinforced phenolic. The horizontal plates were rigidly attached to the support, and the support structure itself served to mount the coil assembly inside the bore of the imager, thereby preventing any bulk coil motions that could arise from the magnetic forces on the wires. The wires themselves were potted securely in the milled grooves using epoxy and were prevented from vibrating loose from these grooves by the next adjacent layer of cooling channels, since all layers were tightly sandwiched together.

Coil Construction

To produce high gradient efficiencies, it is advantageous to use the maximum number of wires possible. This number is constrained in an obvious way by the wire diameter, minimum spacing between wires, and circumference of the cylindrical former. To obtain the desired gradient efficiencies for these coils, it was necessary to use relatively small wires (AWG no. 20) with a diameter of ~1 mm and an interwire spacing of 0.5 mm. The G_x (outermost) coil was wound with a single length of wire such that 216 axially directed segments generated the required current density, and for the G_z (innermost) coil, 200 axially directed segments were wound. For the middle coil (G_y), constraining the closest separation of the wires to be 0.5 mm allowed 48 loops per side. For all three coils, the wire paths were milled (numerically controlled) into the surface of polycarbonate/acrylic formers. Wire was then wound into these grooves and epoxied in place. Figure 4a shows the constructed G_x coil, complete with horizontal plates after winding with (dielectric) insulated copper wire. The upper plates were curved downward at the superior and inferior ends to provide a more comfortable structure for patient support. Figure 4b shows the middle coil (G_y) before assembly of the complete gradient coil unit.

The resistivity of the small-diameter wire used to construct the coils is relatively high, increasing from 33.3 mΩ/m at room temperature to 40.5 mΩ/m at 75°C (our specified upper limit on temperature at the wire). The additional length of wire required to extend the return paths away from the main cylinders also contributed to high coil total resistances. Since high root-mean-squared (RMS) currents are required for the desired imaging applications, the power dissipated by the coils is significant (~1250 W for one coil @ 25A RMS). In a mock-up of one quadrant of a coil, when a 25A RMS current was applied

with no cooling, the temperature of the quadrant rose from 10°C to 100°C in 2.5 minutes. With air cooling only, a temperature rise from 10°C to 35°C in 4 minutes was observed. A more efficient cooling system was therefore required to ensure patient safety.

Water is one of the most efficient and economical cooling fluids available. Its heat capacity (C_p = 4.18 J/g/°C) is approximately two times higher than other commonly available cooling fluids such as hydrocarbon oils (e.g., ethylene glycol). Assuming that all heat generated is transferred to the cooling water and the maximum allowable temperature rise of the water is 5°C, a water flow of 3.6 liter/min is required to remove 1250 W of heat. Conventionally, water-cooling channels for gradient coils are constructed from copper tubing. For a compact gradient coil set, the competing demands of space limitations and the requirement of a large cooling channel cross-section to ensure adequate volume flow rates necessitated the design of a novel cooling system. We designed this cooling system in separate modules, each module corresponding to a quadrant of a single gradient coil. Each module consisted of a skeleton of cooling channel spacers that were milled from a 3.0-mm-thick polycarbonate sheet. This was covered on both sides with a very thin (0.25-mm-thick) polycarbonate film (GE Plastics, General Electric Company, Pittsfield, MA) to allow close thermal contact of the wires with the cooling water while ensuring electrical insulation. The film was bonded to the skeleton using ultraviolet-curing polyvinyl chloride-based bonding adhesive (Loctite 3311, Loctite Corporation, Mississauga, Canada). The tensile strength (to break) of the polycarbonate film was rated at 9000 psi, according to American Standards of Testing Materials (ASTM) D882, and the burst strength was 200 psi (ASTM D774). The modules were tested for flow uniformity and resistance to leaks by flowing water at 13 liter/min for >5 hours before permanent incorporation into the gradient coil structure. After incorporation into the gradient coil set, the modules were connected in parallel to lower the fluid resistance of the network of cooling channels and thereby allow increased water flow rates.

This design allowed very close thermal contact between the wires and water in the cooling channels (while maintaining electrical isolation) and also provided a large surface area over which heat could be transferred to the water. The ability to test the cooling channel integrity separate from the gradient coil structure was vital in ensuring no electrical shorting due to water leakage. An additional benefit of constructing the cooling system from polycarbonate is that no electrical currents can be created in this material, and it is therefore not susceptible to eddy current generation like some copper systems. Since the thickness of the cooling channel module was only 3.5 mm, the maximum total wall thickness of the gradient coil structure was less than 3 cm. The assembled gradient coil structure, including RF coil and water connections, is shown in Fig. 5.

RF Coil

Several cylindrical RF coil designs exist that can be used in a transverse geometry for imaging the breast (i.e., with
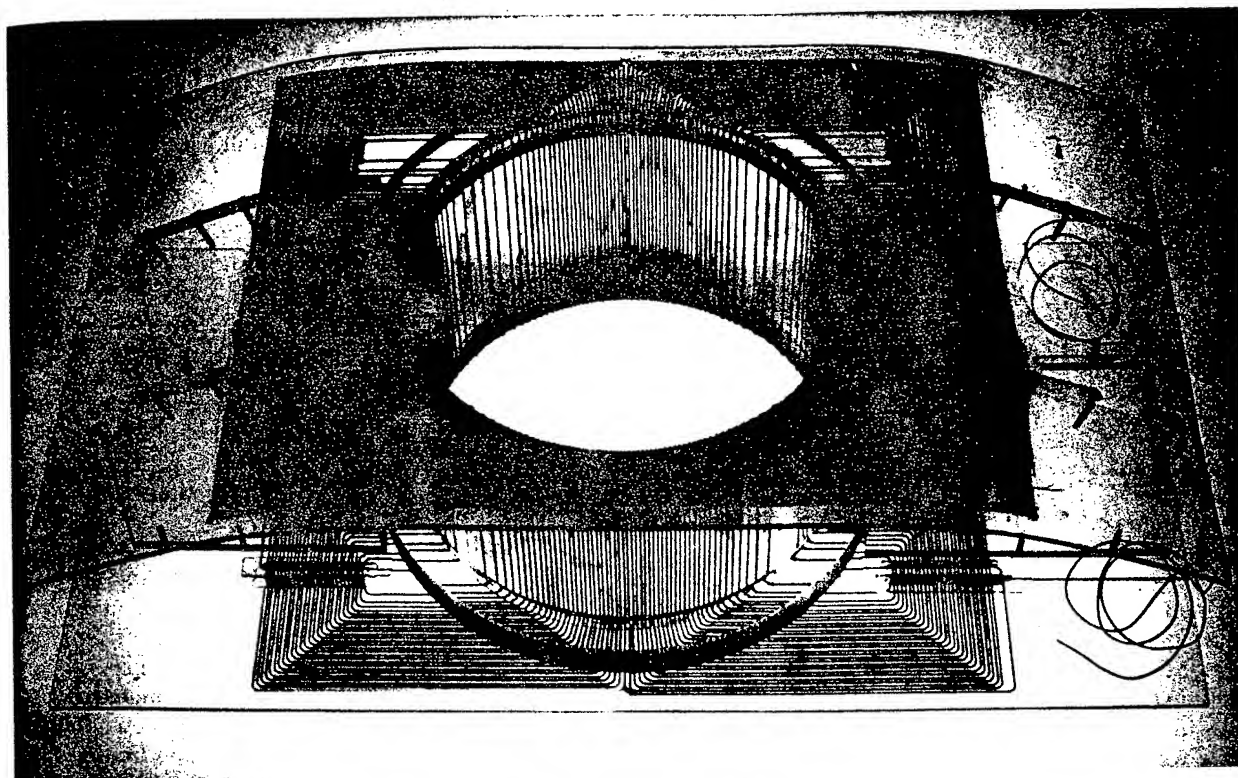
a
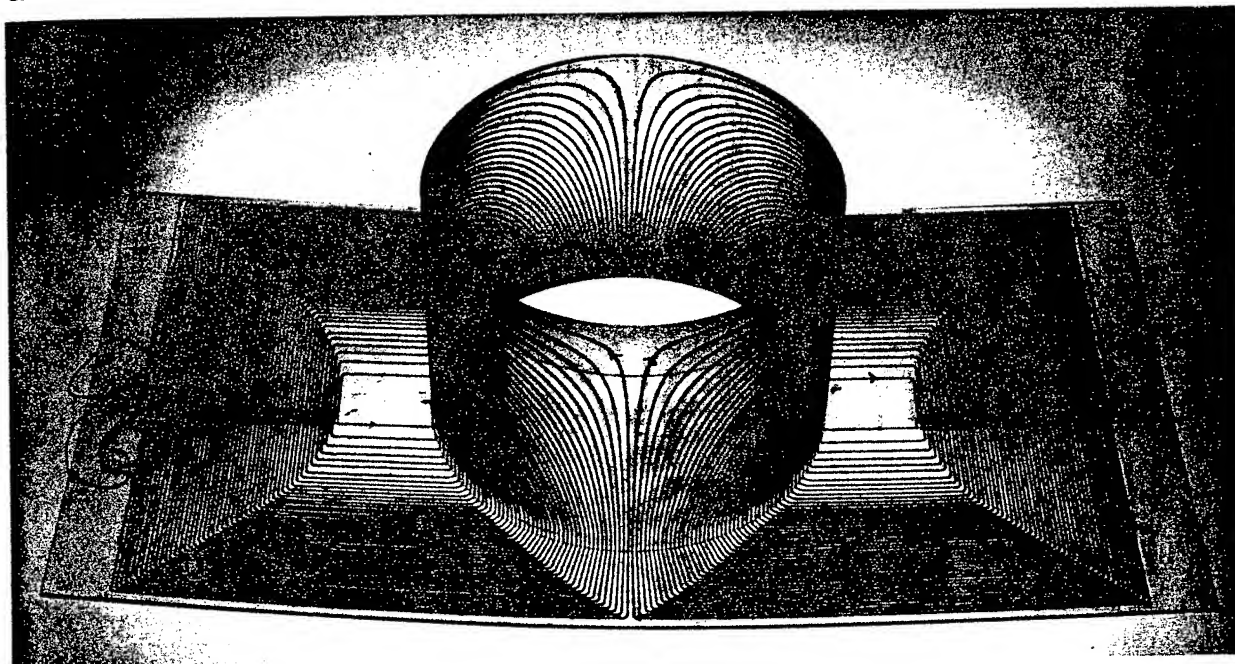
b

FIG. 4. (a) G_x quadrupole coil with 216 windings. (b) G_y coil showing placement of the "return wires" on a horizontal plate.

the coil axis perpendicular to the main magnetic field B_o). These coils, when oriented vertically, produce B_1 fields directed along either the horizontal x direction (e.g., saddle coils (6)) or along the vertical direction (e.g., solenoidal coils (7, 8)).

The construction of an RF coil for operation inside our breast gradient coils is a difficult problem, in that the proximity of the RF coil to the gradient coils results in very strong inductive coupling and detuning of the RF coil (given that the gradient coil radius is constrained to be as small as possible for maximum efficiency). To determine the best RF coil design for our gradient coil set, two different RF coils were constructed and tested. The first coil constructed was a quadrature RF coil with
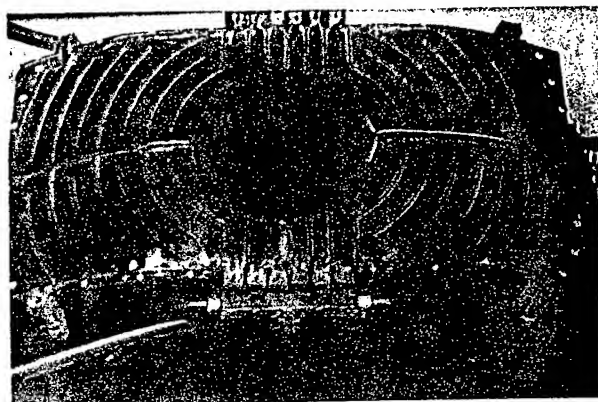
FIG. 5. Assembled gradient coil module showing RF coil and cooling channels.

two separate coils providing the perpendicular B_1 components. In this arrangement, a simple three-loop solenoidal coil provided the vertical mode, and a saddle coil built onto the same former provided the horizontal mode. The second coil constructed was a 16-rung high-pass birdcage RF coil designed for operation in a linear mode (recall that a birdcage coil cannot be used in quadrature mode in the vertical orientation because one of the modes would be parallel to B_0). We chose this design over a saddle-coil arrangement because of the superior uniformity of B_1 produced by the birdcage coil over the volume enclosed by the coil. A split cylindrical RF shield was constructed from fine copper screen and located immediately inside the smallest diameter gradient coil. The coils were tested for coupling to the gradient coils. The quality factors, Q, were measured, and the coil performances were compared.

Diffusion Imaging

Preliminary diffusion measurements were made using a short-T_2 phantom consisting of $NiSO_4$-doped agarose gel ($T_2 = 60$ ms at 1.89 T) with a diffusion-sensitized spin-echo sequence (pulsed gradient spin-echo sequence (9)). Apparent diffusion coefficient (ADC) maps were calculated from a series of 10 diffusion-weighted images with diffusion b factors between 0 and 1000 s/mm². Each of these images was the geometrical average of two images with equal diffusion-weighting but with opposite diffusion gradient polarity to remove the effects of diffusion-weighting cross-terms from interaction between the diffusion and imaging gradients (10). The ADC maps were obtained under three conditions: (1) using the standard whole-body manufacturer-supplied gradient coils for all imaging and diffusion-weighting gradients; (2) using our custom coils for all imaging and diffusion-weighting gradients, with the gradient strengths matched to those of the whole-body coils by applying an appropriately scaled current to the coils; and (3) using our custom coils for all imaging and diffusion-weighting gradients, with the imaging gradient strengths matched to those of the whole-body coils, but taking advantage of the increased gradient efficiency to apply higher strength, shorter diffusion-weighting gradients, thereby shortening the scan TE. In the first two experiments, the minimum TE required for

diffusion weighting of $b = 995$ s/mm² was TE = 80 ms (with diffusion gradient strength of 22 mT/m). TR was set to 600 ms, the matrix size for the scan was 256 × 128, and the image size was 8 × 8 cm, for a total scan time of 2.5 minutes for each image (5 minutes for each b factor). Diffusion gradients were applied along the readout axis, x, for all experiments. For the third experiment, the TE was decreased to TE = 46 ms by increasing the strength of the diffusion-weighting gradient pulses by a factor of four (88 mT/m) to obtain much larger b factors with shorter diffusion pulses. All other parameters (including slice thickness) were matched to the first two experiments.

RESULTS

Coil Performance

The field produced by each of the three coils was calculated by direct numerical solution of the Biot-Savart Law for the wire paths, including return wire contributions. Calculated gradient efficiency for all three coils, together with the measured resistance and inductance, are summarized in Table 1. Contour plots of calculated gradient uniformity for the G_z quadrupole coil are shown in Fig. 6. Figure 6a shows the percentage deviation from gradient uniformity for a y-x plane through the center of the coils. A similar plot is shown in Fig. 6b for a x-z plane, transverse to the coil axis, at a height equal to the center of the VOI (i.e., located 5.9 cm below the top surface of the coils). These plots show the excellent gradient uniformity within the VOI that is predicted for the G_z coil. The gradient strength decreases near the ends of the coil, because the finite length of the coil causes a decrease in field strength. Similar results were obtained for the G_x gradient coil, with appropriate scaling for the number of wires and the coil radius. The performance of the modified target field G_y coil is shown in Figs. 6c and 6d. A larger deviation from gradient uniformity is present for this coil, compared to the G_x and G_z coils. This problem is inherent to any design for a G_y coil in the transverse orientation, since there is an additional gradient in the y direction due to the natural field fall-off that occurs as the ends of the coil are approached. To create a G_y coil with optimum gradient efficiency, we would like to maximize $|B_z|$ at both ends of the coil, with B_z a maximum in the $+z$ direction at one end of the coil, and a maximum in the $-z$ direction at the opposite coil end. The field fall-off inherent in this coil orientation works against the gradient we desire to create, since it necessarily results in a decrease in the magnitude of B_z as the coil ends are approached. Instead of working against the natural field fall-off toward the ends of the coil, we have designed a

Table 1
Coil Performance Characteristics

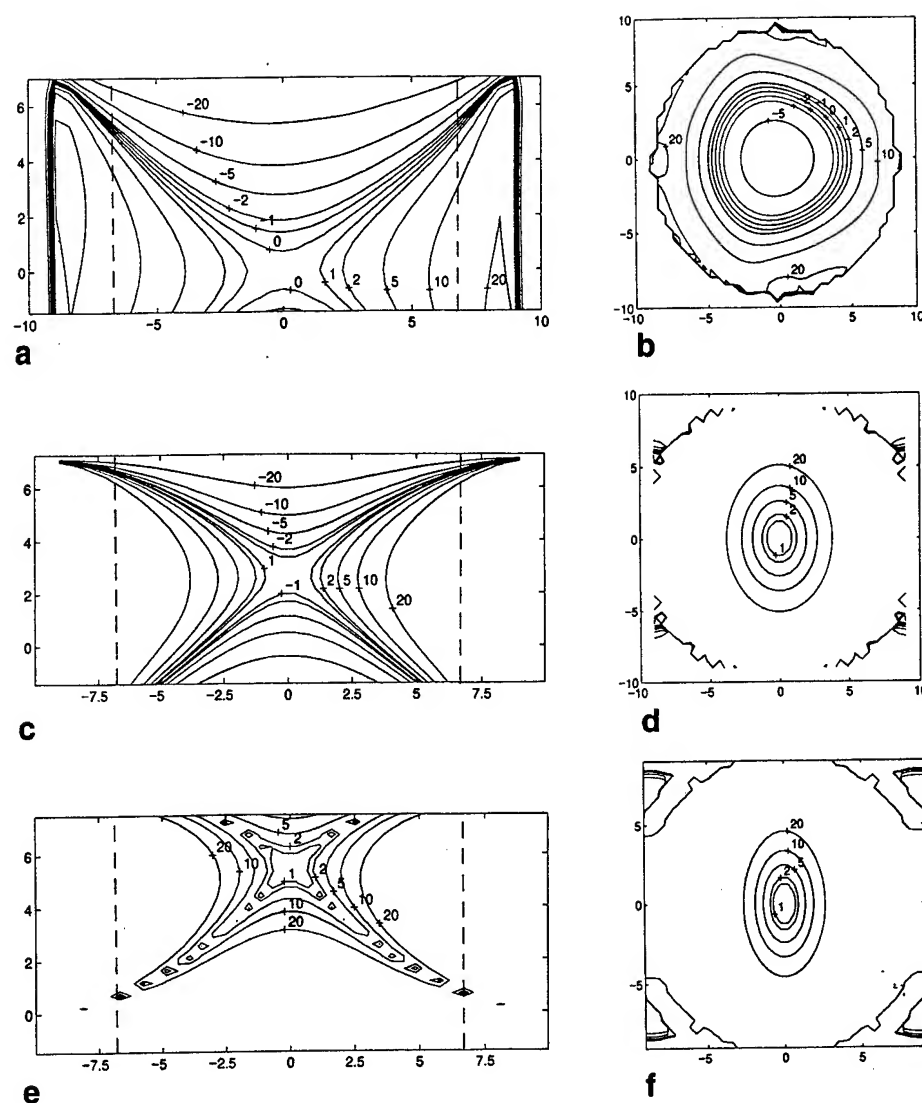|	Mean diameter (cm)	Efficiency (mT/m/A)	Inductance (μH)	Resistance (Ω)
G_x (quadrupole)	21.1	2.9	754	2.3
G_y (fingerprint)	19.5	1.7	829	2.6
G_z (quadrupole)	18.1	3.3	1024	1.9

FIG. 6. Contour plots showing percentage deviations from gradient uniformity for the G_z coil over (a) an axial plane (x-y) showing the entire VOI with the top edge of the plot corresponding to the top surface of the coils. The outer circumference of the VOI is at 6.75 cm, as indicated by dashed lines. (b) A coronal plane (x-z) located at the center of the defined VOI, i.e., at ~3 cm above the geometric coil center. In Fig. 6a, the contours are symmetric around $y = 0$ cm with some small deviations due to return-wire contributions. (c, d) The corresponding plots for the constructed G_y coil shown in Fig. 4b. (e, f) The corresponding plots for a conventional transverse coil with return wires on the cylinder, as in Fig. 3b.

coil to produce $B_z = 0$ at the upper end of the coil, and a maximum in B_z toward the bottom end, similar to the asymmetric head coil design by Roemer (11). We used the target field approach to optimize the rate at which the field falls off toward the upper end of the coil to produce a linear variation in B_z. Although the region of acceptable gradient uniformity for our truncated target field coil is not as large as for the quadrupole coils, it compares favorably to the performance of the full target field design. We show in Figs. 6e and 6f the corresponding plots from a complete 40 loop per side target field coil with the same dimensions as our modified coil (i.e., with return wire paths at the bottom of the cylinder as in Fig. 3b). The region of acceptable gradient uniformity for our truncated target field coil is much larger than for the complete target field coil. In addition, the gradient efficiency is better for our truncated coil by a factor of 1.7, due to

the larger number of windings that could be placed on the cylinder for our coil.

To verify the field simulations, gradient uniformity was tested by acquiring images of grid phantoms. Deviations from gradient uniformity are manifest in the images as geometric distortions. The phantoms consisted of acrylic cylinders filled with square plastic gridding and $CuSO_4$-doped 0.9% saline solution. The grid spacing was 1.7×1.7 cm, whereas the phantoms had an outer diameter of 12.5 cm and a height of 15 cm (extending 3 cm higher than the top surface when placed inside the coils). The coil performance was tested on a clinical GE Signa imager, using our coils for all imaging gradients (with gradient strengths matched to the whole-body coils) in a standard spin-echo pulse sequence. In general, local gradient coils often require modification of the compensation network for the gradient coil amplifiers since the

coil inductances are quite different from the whole-body coils. Because the inductances of our breast coils were very similar to the whole-body coils, no modification of the network was necessary. Images of a grid phantom are shown in Fig. 7 for planes corresponding approximately to the theoretical field plots shown in Figs. 6a and 6b and are evidence of the good gradient uniformity achieved over most of the VOI. These images were acquired using a spin-echo sequence with TE = 20 ms, TR = 500 ms, matrix size = 256 × 256, and 2 NEX. The image size is 16 × 16 cm, and the VOI vertical extent is marked with arrows.

The first RF coil we constructed was a quadrature coil consisting of a solenoidal coil to provide the vertical mode and a saddle coil to provide the horizontal coil. Unfortunately, the vertical mode was inductively coupled to both the y-gradient coil and to the RF shield and could not be tuned to the proton resonant frequency at 1.5 T. We therefore chose to construct a coil that would operate in linear mode, with only a horizontal B_1 component present. We constructed a birdcage coil that creates a horizontal mode B_1 field with a high degree of homogeneity over a large volume. The unloaded Q of this coil (when located inside the gradient coil structure) was 80, whereas the Q for loading with a 0.9% saline phantom was 29.

Although the gradient strengths required for conventional imaging (10 mT/m) can be generated at less than 6 A using these coils, higher currents are required for more demanding applications such as flow imaging and diffusion imaging. To test the effectiveness of the water cooling system, a DC current was applied to the coil with the highest total resistance, G_y, and the temperature rise was measured for different water flow rates by monitoring a thermocouple located on the surface of the wires. The temperature was monitored until equilibrium was

achieved. Measured temperature rises are shown in Fig. 8 for DC currents between 0 and 22 A and a cooling water flow rate of 8 liter/min. Similar results were obtained for other flow rates, at which the equilibrium temperature increased with decreasing flow rates but did not change significantly from the results shown in Fig. 8 for higher flow rates. This behavior has also been demonstrated in purely cylindrical gradient coils and was modeled by Chu and Rutt (12) using an analysis based on fundamental heat transfer theory.

Diffusion Imaging

ADC maps for a T_2 = 60 ms NiSO$_4$-doped agar phantom are shown in Fig. 9; Fig. 9a shows the results obtained using the GE gradient coils, and Fig. 9b shows the results obtained using our gradient coils with diffusion gradient strengths four times higher than that of the GE coils. The mean ADC for all three experiments was the same within experimental error: $(1.8 \pm 0.3) \times 10^{-3}$ mm^2/s for the GE coils ($\pm 30\%$ peak-to-peak), $(1.8 \pm 0.3) \times 10^{-3}$ mm^2/s for our gradient coils with diffusion gradient strengths matched to the GE coils, $(1.9 \pm 0.2) \times 10^{-3}$ mm^2/s for our gradient coils with diffusion gradient strengths four times higher than that of the GE coils and TE = 46 ms. As expected, the observed signal-to-noise ratio was increased by nearly a factor of 2 for the TE = 46 ms images compared to the corresponding b-factor images at TE = 80 ms.

DISCUSSION

The performance and homogeneity of the gradient coils were in excellent agreement with theoretical predictions. The volume of acceptable gradient uniformity (<20% deviation) extended over most of our defined VOI for all
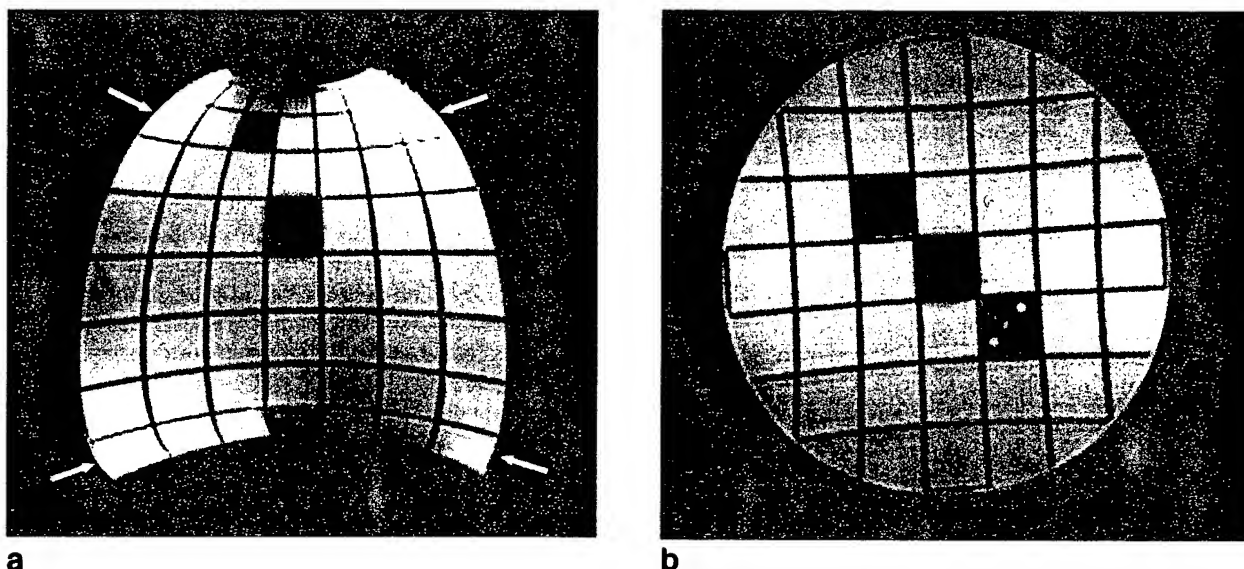

a   **b**

FIG. 7. Spin-echo images of a grid phantom acquired (a) for an axial plane (x-y) and (b) for a coronal plane (x-z) with the specialized breast quadrupole gradient coils. The input current strength required for the least efficient (G_y) coil was approximately 14 times less than that required for the corresponding GE coil.
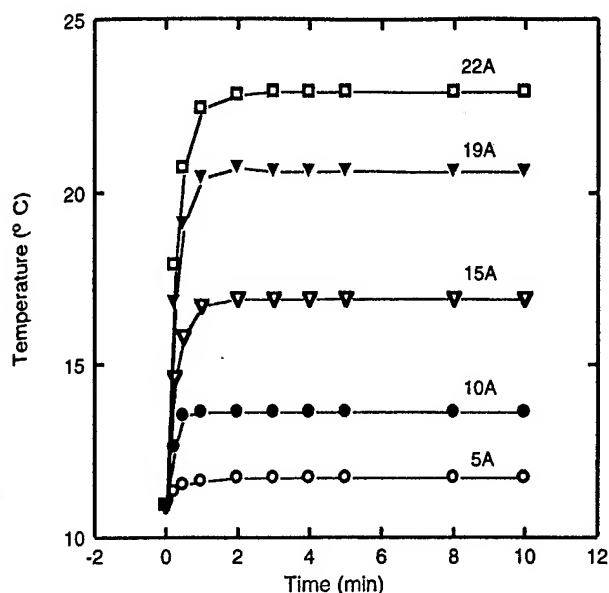
FIG. 8. Temperature response of assembled gradient coils to a DC current applied to the coil with the highest resistance (G_y) monitored at the surface of the G_y coil where the winding density was greatest.

three gradient coils. For this region, the theoretical plots of B_z can be used to generate a gradient-warping algorithm for the coils (13) to correct spatial distortions in the images. Additionally, the known deviations from gradient uniformity can be used to correct calculations of diffusion-weighting b factors (which will vary spatially across the VOI for our coils). Unfortunately, greater deviations from uniformity could not be avoided for the top 1 cm of the VOI near the upper edges of the coils for our coil designs. Deviations from uniformity of more than 20% lead to large image distortions and likely cannot be satisfactorily corrected using conventional schemes. Many breast lesions occur close to the chest wall; to be clinically useful, it is important to image accurately as close to the chest wall as possible. Several new gradient coils with improved gradient uniformity at the top edge of the coil have been reported recently (14, 15). Future improvements on our coil design will focus on extending the region of usable gradient beyond the top edge of the coil (16) as far as possible. For our preliminary clinical work with these coils, we will limit our study to patients with known lesions occurring in a region of the breast that falls within the 20% uniformity region of our gradient coils. This approach will allow us to implement pulse sequences under ideal conditions, (a) to determine the best parameters for visualizing breast lesions, (b) to determine the minimum required gradient strengths and uniformities, and (c) to make an initial assessment of the clinical utility of this approach.

In future coil designs, it may be possible to extend the region of usable gradient farther into the cylinder in the $-y$ direction by recessing the coils in the patient table or by constructing a dedicated breast imaging table, thereby allowing higher aspect ratio coils. In this design, the coil assembly would be constructed to allow positioning on either side of the table, depending on which breast was being imaged. A fiberglass or Kevlar sheath covering the coil assembly and running the length of the patient table would serve the dual functions of isolating the patient from the electrical and cooling circuits and providing an additional form of mechanical fixation to secure the coils on the table. Because the coils are not torque-balanced, it will be necessary to anchor the structure firmly, both from the point of view of vibration-induced imaging artifacts and of patient safety.

The high gradient efficiencies of these coils will allow much higher spatial-resolution imaging than can currently be achieved in a clinical setting, and additionally, will provide very large amplitude motion-sensitizing gradients, thus facilitating diffusion imaging (or flow imaging) in small blood vessels with short echo times. T_2 has been measured for human breast tissue, with reported values ranging between 60 and 150 ms (17, 18). Recently, we reported T_2 approximately 70 ms for human breast tumor (MCF7 human breast carcinoma) growing in a mouse mammary fat pad (19). More fibrous tumors can have significantly shorter T_2s. For this reason, initial signal loss at $b = 0$ s/mm^2 due to T_2 weighting of the image can severely limit the range of b factors for which images can be obtained, which has the result of limiting the precision of the ADC measurement. Our approach is to shorten TE while maintaining diffusion weighting by increasing diffusion gradient amplitudes. This gives a substantial increase in initial signal intensity for $b = 0$ s/mm^2, allowing high-quality images to be obtained for much higher b factors. Even in cases in which signal loss from T_2 weighting is not so severe as to limit ADC precision, the ability to obtain high diffusion weighting with short TE reduces dramatically the T_2 contrast in an image. This will allow acquisition of a diffusion-weighted image in which the contrast is determined mainly by tissue ADC rather than by a mix of ADC and T_2.

A secondary important benefit that can be gained using high-efficiency gradient coils is that the ramp time required to attain imaging gradient strengths (10–25 mT/m) is decreased from that required by whole-body coils by a factor of the efficiency (since the current slew rate is similar to whole-body coils, and the required peak current is decreased). This will enable echo-planar imaging (and other fast imaging techniques) using conventional gradient amplifiers. Echo-planar imaging techniques have been proven to be much less susceptible to motion artifacts than conventional imaging sequences (20) and have recently been applied to diffusion imaging in vivo (21) with good results.

For rapid imaging pulse sequences, and for high-amplitude bipolar pulses, very rapid changes in gradient polarity are required. Although the magnetic field amplitudes drop off quickly in the region above the coils, magnetic fields are also generated by the return wires on the horizontal plate, and excitation thresholds for cardiac stimulation must be considered. As an upper limit for one coil, $|B|$ was calculated for the G_z coil at various distances above the return wires at the location of the highest wire density. The maximum dI/dt from our gradient coil amplifiers is 200 A in 184 μs. This produces dB/dt = 156 T/s at 1 cm above the coil return wire plate
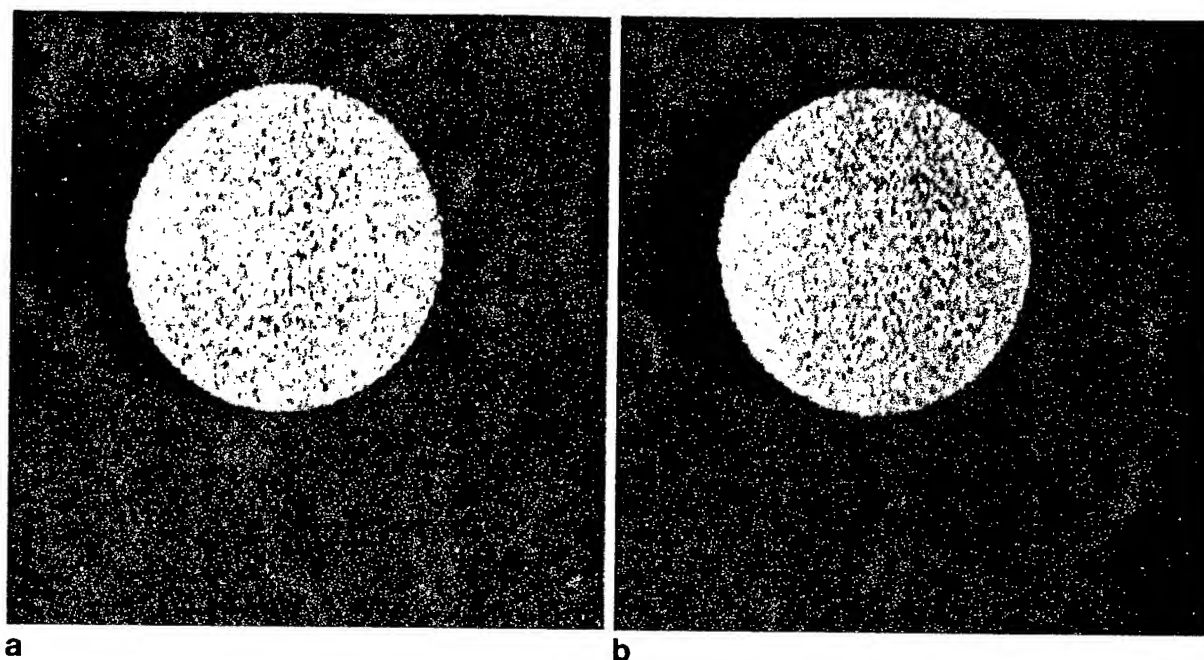
FIG. 9. ADC maps of a $T_2 = 60$ ms agar phantom obtained (a) using the whole-body coils to provide all diffusion and imaging gradients, TE = 80 ms, and (b) using the breast gradient coils to provide all gradients, where the diffusion gradient strengths were four times the whole-body gradient strengths and TE = 46 ms. In all cases, the ADC maps were constructed from 10 images with $b = 0$ to $b = 1000$ s/mm^2.

and dB/dt = 50 T/s at 10 cm, compared to a recommended upper limit of 400 T/s for cardiac stimulation (22). The magnitude of these fields is relatively small at regions of concern with respect to magnetic stimulation such as the heart; however, peripheral nerve stimulation has been reported at dB/dt as low as 40 T/s in some patients (22). Theoretical field calculations will allow prediction of $|B|$ and dB/dt for all pulse sequences before implementation, and pulse sequences will be tailored to adhere to maximum dB/dt and peak $|B|$ guidelines. Additionally, if peripheral nerve stimulation is reported for individual patients, dB/dt will be reduced below the stimulation threshold by increasing gradient switching times.

SUMMARY

We have constructed a three-axis gradient coil set for imaging human breast tumors. These coils create gradient efficiencies of up to 3.3 mT/m/A with relatively low inductance (≤ 1000 μH), and good gradient uniformity over most of the volume required for breast imaging. Preliminary diffusion results were obtained in a water phantom for b factors as high as ~1000 s/mm^2 for TE = 46 ms. A compact, efficient water-cooling system was presented, which maintained coil temperatures at or below room temperature, even for RMS currents as high as 20 A. This gradient/cooling module will allow, for the first time, clinical breast imaging using diffusion and microvascular flow-weighted protocols with high spatial resolution.

REFERENCES

1. D. S. Webster, K. H. Marsden, Improved apparatus for the NMR measurement of self- diffusion coefficients using pulsed field gradients. *Rev. Sci. Instrum.* **45**, 1232–1234 (1974).
2. K. C. Chu, B. K. Rutt, Quadrupole gradient coil design and optimization: a printed circuit board approach. *Magn. Reson. Med.* **31**, 652–659 (1994).
3. W. G. O'Dell, J. S. Schoeniger, S. J. Blackband, E. R. McVeigh, A modified quadrupole gradient set for use in high resolution MRI tagging. *Magn. Reson. Med.* **32**, 246–250 (1994).
4. R. Turner, A target field approach to optimal coil design. *J. Phys. D. Appl. Phys.* **19**, L147–151 (1986).
5. R. Turner, Gradient coil design: a review of methods. *Magn. Reson. Med.* **11**, 903–920 (1993).
6. P. W. McOwan, T. W. Redpath, A specialised receiver coil for NMR imaging of female breasts. *Phys. Med. Biol.* **32**, 259–263 (1987).
7. J. P. Hornak, J. Szumowski, R. G. Bryant, Elementary single turn solenoids used as the transmitter and receiver in MRI. *Magn. Reson. Imaging* **5**, 233–237 (1987).
8. L. Sun, L. O. Olsen, P. L. Robitaille, Design and optimization of a breast coil for magnetic resonance imaging. *Magn. Reson. Imaging* **11**, 73–80 (1993).
9. E. O. Stejskal, J. E. Tanner, Spin diffusion measurements: spin echoes in the presence of a time-dependent field gradient. *J. Chem. Phys.* **42**, 288–292 (1965).
10. M. Neeman, J. P. Freyer, L. O. Sillerud, A simple method for obtaining cross-term-free images for diffusion anisotropy studies in NMR microimaging. *Magn. Reson. Med.* **21**, 138–143 (1991).
11. P. B. Roemer, Transverse gradient coils for imaging the head. United States Patent No. 5177442, January 5, 1993.
12. K. C. Chu, B. K. Rutt, MR gradient coil heat dissipation. *Magn. Reson. Med.* **34**, 125–132 (1995).
13. M. O'Donnell, W. A. Edelstein, NMR imaging in the presence of magnetic field inhomogeneities and gradient field nonlinearities. *Med. Phys.* **12**, 20–26 (1985).
14. A. Ersahin, H. K. Lee, O. Nalcioglu, Asymmetric gradient coil design for high resolution breast imaging, in "Proc., SMR and ESMRMB, 3rd

Annual Meeting, Nice, 1995," p. 954.

15. H. K. Lee, R. Raman, R. Slates, A. Ersahin, O. Nalcioglu, An optimized gradient coil for breast imaging, *in* "Proc., SMR and ESMRMB, 3rd Annual Meeting, Nice, 1995," p. 955.

16. B. A. Chronik, B. K. Rutt, Constrained length minimum inductance gradient coil design, *in* "Proc., ISMRM, 5th Annual Meeting, Vancouver, B.C., Canada, 1997," p. 53.

17. D. Z. J. Chu, W. S. Yamanashi, J. Frazer, C. F. Hazlewood, H. S. Gallager, A. W. Boddie, R. G. Martin, Proton NMR of human breast tumors: correlation with clinical prognostic parameters. *J. Surg. Oncol.* **36**, 1–4 (1987).

18. S. J. Graham, M. J. Bronskill, J. W. Byng, M. J. Yaffe, N. F. Boyd, Quantitative correlation of breast tissue parameters using MR and X-ray mammography. *Br. J. Cancer* **73**, 162–168 (1996).

19. C. F. Maier, Y. Paran, P. Bendel, B. K. Rutt, H. Degani, Quantitative diffusion imaging in implanted human breast tumors. *Magn. Reson. Med.* **37**, 576–581 (1997).

20. R. Turner, D. LeBihan, Single-shot diffusion imaging at 2.0 Tesla. *J. Magn. Reson.* **86**, 445–452 (1990).

21. R. Turner, D. LeBihan, A. S. Chesnick, Echo-planar imaging of diffusion and perfusion. *Magn. Reson. Med.* **19**, 247–253 (1991).

22. J. P. Reilly, Principles of nerve and heart excitation by time-varying magnetic fields, *in* "Biological effects and safety aspects of NMRI and spectroscopy." *Ann. N. Y. Acad. Sci.* **649**, 96–107 (1993).